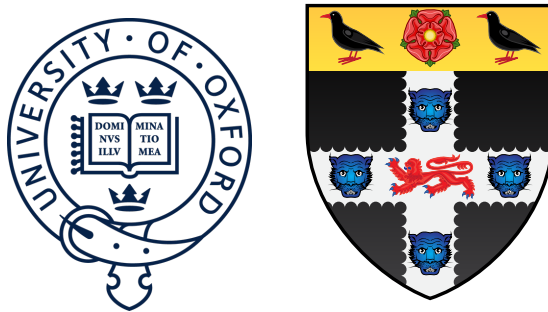


First Measurement of the Solar Neutrino Oscillation Parameters via Boron-8 Solar Neutrinos in SNO+



Daniel Cookman

Christ Church College

University of Oxford

A thesis submitted in fulfilment of the requirements for the degree of

Doctor of Philosophy

Trinity Term 2022

To my parents

and

To Oscar Jacobsson:

The best of us

Acknowledgements

And I would like to acknowledge ...

Abstract

Formal 1-page summary of the work completed in the thesis.

Table of contents

List of Figures

List of Tables

List of Acronyms

SNO Sudbury Neutrino Observatory

Introduction

Couple of pages outlining document's structure and contents (this is what each of the chapters is here for). Less formal than the abstract, also explaining what the expected audience of this thesis is: who will find this document useful!

1

2

3

4

Chapter 1

5

The Theory of Neutrino Physics

6

*Light**Light**The visible reminder of Invisible Light*

7

The Rock

T. S. ELIOT

1.1 The Standard Model and Neutrinos

8

1.1.1 A Brief Introduction to the Standard Model

9

Covering how the SM works at the highest level, including:

10

- Quantum Field Theory and the Lagrangian dynamical framework
- The connection between symmetries of a QFT model and its gauge fields that describe the model's forces
- The SM's fundamental symmetries, and associated forces, but —

11

12

13

14

- Not (exactly) what we see “normally”! The electromagnetic and weak forces appear distinct, and the weak gauge bosons have mass. To explain this, we need a further component, the Brout-Englert-Higgs (BEH) Mechanism. 15
16
17

[2 pages total] 18

1.1.2 Neutrinos within the Standard Model 19

- Basic description of where neutrinos fit into SM: 3 kinds of neutral fermion, the counterparts to the charged fermions. Interacts with the weak force only. 20
21
- Summary of the experimental evidence for this picture: mainly, the discovery of electron anti-neutrinos by Cowan and Reines, the muon neutrino by Lederman, Schwartz, and Steinberger, and the tau neutrino by the DONUT Collaboration. Further critical experiments include the first measurement of a neutrino’s helicity by Goldhaber et al. as well as Danby et al.’s demonstration that ν_μ are distinct from ν_e . 22
23
24
25
26
27
- More detailed description, via Feynman diagrams, of the two fundamental modes of interaction by neutrinos with the weak force: charged- and neutral-current interactions. A brief mention of the quantitative theory that underlies description: Gashow, Salam, and Weinberg’s Electroweak Theory. This explains not only the V–A structure of charged-current interactions, but also predicted accurately the nature of neutral-current interactions. (Given space constraints, I see no reason to go into much of the details of the theory, or the many experimental tests of its structure.) 28
29
30
31
32
33
34
35

[4 pages] 36

1.2 Neutrino Oscillations and Neutrino Masses	5
1.2 Neutrino Oscillations and Neutrino Masses	37
1.2.1 The Evidence for Neutrino Oscillations	38
• Describe status quo ante of massless nature of neutrinos: BEH mechanism as exists cannot allow for neutrinos to have mass as only left-handed neutrinos have been observed.	39 40 41
• Furthermore, strong experimental limits on neutrino masses, from e.g. tritium-decay endpoint measurements by the KATRIN experiment and cosmological inferences from the CMB by the Planck satellite.	42 43 44
• But — then neutrino oscillations are observed over a variety of experiments and contexts. Summarise critical bits of evidence:	45 46
• Electron neutrino disappearance in solar neutrino experiments, including Ray Davis' Homestake experiment, the SAGE/GALLEX experiments, and SNO. For the latter, the comparison of charged-current and neutral-current modes of interaction was clear evidence of neutrino oscillations over other types of process (e.g. neutrino decay).	47 48 49 50 51
• Include in the above a brief description of Bahcall's Standard Solar Model.	52
• Muon neutrino disappearance in atmospheric and long-baseline accelerator neutrino experiments, such as Super-Kamiokande, T2K, and No ν a.	53 54
• A few further observations to note are: reactor electron anti-neutrino disappearance from both KamLAND and Daya Bay; tau neutrino appearance at the OPERA experiment; short-baseline neutrino anomaly within LSND and MiniBooNE (with recent contrary evidence from MicroBooNE).	55 56 57 58
[5 pages]	59

1.2.2 The Phenomenology of Neutrino Oscillations	60
• Describe the current phenomenological model of 3-flavour neutrino oscillations that can explain all of this evidence: the PMNS mixing matrix.	61 62
• Describe also the MSW effect, which is critical for explaining solar neutrino oscillations.	63 64
• Show the formula for solar neutrino oscillations, given this MSW effect in both the Sun and Earth. Note the dependence of solar neutrino oscillations on only the “solar” oscillation parameters. This is all particularly useful for the solar analysis chapter.	65 66 67 68

$$P_{ee} \left(\tan 2\theta_{12}^M, \sin \theta_{13}^M, \Delta m_{21,M}^2 \right) = BLAH \quad (1.1) \quad 69$$

[3 pages]	70
-----------	----

1.2.3 The Origins of Neutrino Mass	71
---	----

• Observed neutrino oscillations require at least two neutrino mass states to be non-zero. Given constraints of the current SM, two main ways of adding neutrino masses: a Dirac mass term (i.e. allowing for sterile neutrinos), and a Majorana mass term.	72 73 74 75
• For latter, briefly describe what a Majorana particle is, and how with the Seesaw Mechanism (just the simple Type 1 described in-text) one can not only get neutrino masses but also explain their lightness relative to the other massive SM particles. Note that there exist more elaborate versions of this theory.	76 77 78 79
• Furthermore, with reference to the Sakharov conditions, describe qualitatively how the Seesaw Mechanism also allows for possible leptogenesis/baryogenesis in the early Universe, and hence could explain its matter-antimatter asymmetry.	80 81 82

1.2 Neutrino Oscillations and Neutrino Masses

7

• Describe briefly the nuclear physics behind double-beta decay (i.e. why it can happen at all over just normal beta decay), and then how Majorana neutrinos allow for neutrinoless double beta decay, $0\nu\beta\beta$.	83
• Describe the experimental signature of $0\nu\beta\beta$: a spike of events of observed energy equal to the Q-value of the decay.	86
• Note Schecter-Valle Theorem ensures that any observation of $0\nu\beta\beta$ must be the result of neutrinos being Majorana. I.e. the Universe cannot conspire against us and have $0\nu\beta\beta$ without Majorana neutrinos.	88
• Very briefly note the current status of the search for $0\nu\beta\beta$, describing the main varieties of experimental setup seen, along with a nice canonical example of such an experiment and their best limit. In particular, the Germanium-crystal detectors such as GERDA, Xenon-TPC detectors like EXO-200, and large-scale liquid scintillators such as KamLAND-Zen.	91
[3 pages]	96
[CHAPTER TOTAL: 17 pages]	97

Chapter 2

98

The SNO+ Detector

99

The light-soaked days are coming.

100

JOHN GREEN

2.1 Detector Geometry and Design

101

The SNO+ detector is a large, multi-purpose neutrino detector built in the SNOLAB underground laboratory near Sudbury, Canada. Its main detector structure is taken from the Nobel prize-winning Sudbury Neutrino Observatory (SNO) [], which can be seen in Fig. ???. The bulk of the detector is the main detector medium, which changes depending on the phase of the experiment — more on the specifics of this shortly. This medium is held within a 12 m diameter sphere known as the Acrylic Vessel (AV). The AV floats within a body of ultra-pure water (UPW), beyond which is a stainless steel support structure (PSUP) that holds ~ 9000 Photomultiplier Tubes (PMTs). It is these PMTs that detect the light generated from physics events that occur within the detector medium. The AV is kept in place relative to the PSUP through a series of ‘hold-up’ and ‘hold-down’ tensylon ropes. All of these components are suspended within a large cylindrical cavity also filled with UPW. Directly above the detector is

102

103

104

105

106

107

108

109

110

111

112

113

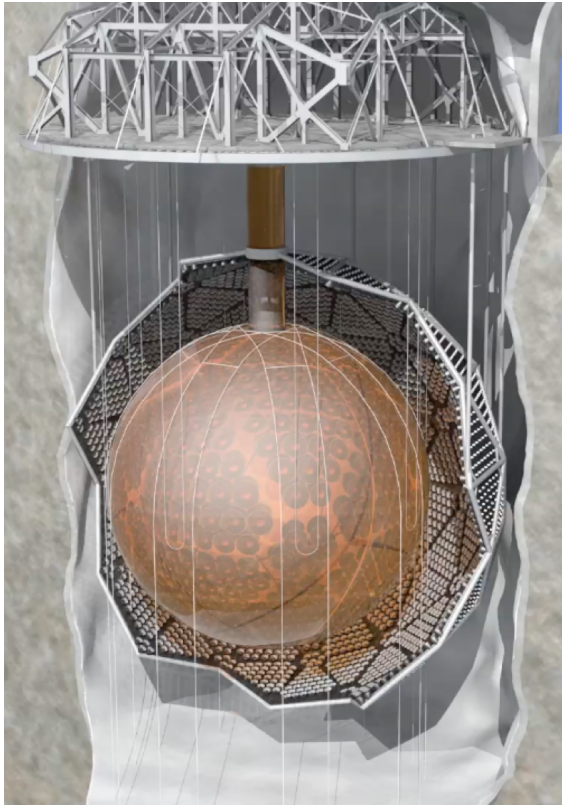


Fig. 2.1: 3D model of the SNO+ detector [?].

the Deck, within which all the detector electronics are kept. Access within the AV for calibration tools and filling is possible only through the acrylic ‘neck’ on top of the AV. This choice of design is highly deliberate, with the details are discussed in [?]. The location 2.2 km underground ensures that there is minimal impact from cosmic rays: only 3 cosmic ray muon events are expected within the detector an hour []. By making the detector spherical, the high degree of symmetry can easily be taken advantage of in event reconstruction and analysis. Moreover, light produced throughout most of the body of the AV will be minimally-impacted by refraction through the acrylic. The only major exception to this is light emitted within ~ 50 cm of the AV, at which point total internal reflection becomes possible. In order to make as much emitted light be able to get detected as possible, all materials within the PSUP were chosen for their optical transparency (excepting the ropes).

2.2 Experimental Phases**11**

Another major design consideration is that of radioactive backgrounds. Maintaining minimal levels of backgrounds is critical for effective particle physics, otherwise the signal one is searching for would become completely swamped. Materials within the detector were chosen to ensure these background levels would be low enough for the Collaboration’s physics goals to be achieved. Another benefit of the spherical design is its high volume-to-surface area ratio, which means that the relatively-high background levels of the PMT glass are kept far away from the detection medium.

126
127
128
129
130
131
132**2.2 Experimental Phases**133
134
135
136
137
138
139
140

As mentioned earlier, SNO+ was designed to fulfil a number of physics goals over multiple ‘phases’ of the detector’s lifetime. The phases are distinguished by the medium that fills the AV. The first main phase (after a brief ‘air-filled’ phase used only for detector commissioning) was that of the ‘water-fill’, with data taken between May 2017 and July 2019. This was used to perform fundamental optical calibrations of the detector [], measurements of the solar neutrino flux [], observation of neutrino oscillations in reactor anti-neutrinos [], and searches for nucleon decay [].

After this, the detector was filled with 800 tonnes of liquid scintillator known as linear alkylbenzene (LAB), mixed with the fluor PPO. More information on the physics of scintillators can be found in Section ???. Filling of the LABPPO cocktail had to be paused in March 2020 due to the COVID-19 pandemic, leading to the detector having its bottom half still filled with UPW, and the top half filled with LAB and PPO at 0.5 g/L. This impromptu phase became known as the ‘partial-fill’, and allowed for some creative analyses to be performed: an initial neutrino oscillation analysis from reactor anti-neutrinos [], as well as the first ever observation of directionality in a high light yield scintillator []. Eventually, filling of the detector with liquid scintillator was able to resume, being completed in May 2021. At that point, the concentration of PPO in the

141
142
143
144
145
146
147
148
149
150

detector was at 0.6 g/L, markedly below the target level of 2.0 g/L. A further ‘PPO’ top-up’ campaign then proceeded, finishing in April 2022 with a final concentration of 151
 2.2 g/L PPO. Thus began the ‘scintillator-fill’ of the experiment, which continues on 152
 during the time of writing. The main goals for this phase include a number of solar 153
 neutrino analyses (including the one described in Chapter ??), a precision measurement 154
 of the neutrino oscillation parameter Δm_{21}^2 using reactor anti-neutrinos [], and further 155
 calibrations of the detector and its backgrounds. 156
 157

Finally, in the near future the detector will be loaded with Tellurium, allowing for 158
 the flagship analysis of the experiment to begin: neutrinoless double beta decay. The 159
 details of this chemical loading process are described in []. Alongside the Te-loaded 160
 liquid scintillator will be a number of other chemicals within the scintillator cocktail 161
 that will help ensure optimal optical properties and chemical stability. These include: 162
 the surfactant DDA to ensure the solubility and stability of the ‘Te-diol’ within the 163
 LAB; the wavelength-shifter BisMSB to absorb light at short wavelengths and re-emit 164
 closer to the optimal quantum efficiency of the detector’s PMTs; and the anti-oxidant 165
 BHT to prevent any free-radicals within the liquid scintillator from ‘yellowing’ the 166
 medium. 167

2.3 Detecting and Recording an Event in SNO+: 168

A Journey 169

To understand well the SNO+ detector, it is worth thinking about how the information 170
 of a physics event, e.g. a solar neutrino interaction, gets observed. This section follows 171
 the journey of such an event. 172

2.3.1 Particle Interactions with Matter

173

All observable physics events within the detector begin by the generation of some form of ionising radiation: α , β^\pm , γ , p or n . These can be created via numerous processes, both exciting (e.g. $0\nu\beta\beta$ or interactions of neutrinos) and banal (e.g. decay of background radioisotopes): see Section ?? for some of them. Regardless of their origin, these particles begin propagating through the detector, and interacting with the detector medium. A number of mechanisms then allow for the generation of optical-wavelength light as a result of these interactions.

180

Cherenkov Light Emission

181

Whenever a charged particle passes through a dielectric medium, nearby molecules polarise and attempt to align their dipoles in the direction of the charge. This results in a temporary polarisation of the medium as the charge passes though it. However, the molecules can only respond to the charge's movement at the speed of light in the medium, which is necessarily slower than the speed of light in a vacuum by a factor of the medium's refractive index. If the charged particle is able to move at a speed greater than the speed of light in the medium, then the dipoles formed within the medium struggle to respond to the motion. This superluminal motion results in a wake of polarisation in the medium, which propagates outwards from the direction of the charged particle: this is Cherenkov light. This process is much akin to the ‘sonic boom’ that occurs when an object travels at supersonic speeds.

192

Cherenkov light emanates outwards in a cone along the direction of the charge's travel; the angle of the cone θ_γ is purely a function of the speed of the charged particle relative to the speed of light, β , and the refractive index of the medium $n(\lambda)$: $\cos \theta_\gamma(\lambda) = \frac{1}{n(\lambda)\beta}$. This formula also demonstrates that there is a minimum speed necessary for Cherenkov light to be generated: $\beta = 1/n(\lambda)$.

197

All detection media are capable of allowing for Cherenkov light to be generated, as 198 long as sufficiently high energy particles can be produced. In the water-fill phase of 199 the detector, Cherenkov light was the only means by which light could be generated. 200 Light from Cherenkov emission can still be created in liquid scintillator, but it tends 201 to be swamped by another form of light generation: scintillation. 202

Scintillation

Whenever a high-energy particle passes through a medium, interactions between the 204 particle and the medium's molecules lead to an inexorable transfer of energy from the 205 former to the latter. These interactions are numerous, and are a function of the type 206 of particle and its kinetic energy. For example, a 5 MeV electron loses energy from 207 electromagnetic interactions with nearby molecules as it passes through, and scatters 208 after colliding with atomic electrons or nuclei. From the perspective of the medium, 209 its molecules use this new-found energy for a number of activities: 210

1. Exciting atomic electrons into various higher-energy states; 211
2. Ionising atomic electrons; 212
3. Increasing the overall kinetic energy of the molecule. 213

At the macroscopic level, process ?? is simply the conversion of the high energy 214 particle's energy into heating the medium. In fact, within most materials the other 215 processes also end up doing the same. 216

However, for certain special classes of material the excitation and ionisation of 217 electrons can lead to a unique process: scintillation (often generally referred to as 218 'luminescence' or 'fluorescence'). Here we choose to focus on the particular case of 219 organic liquid scintillators, given that this is the type of scintillator which currently fills 220 the SNO+ detector. Certain organic compounds (i.e. molecules built from a skeleton 221

Fig. 2.2**Fig. 2.3**

of carbon atoms) have ‘ π -bonds’ in addition to the single ‘ σ -bond’ that is needed to bond two carbon atoms together. A major example of these π -bonds is in the benzene rings of ‘aromatic’ hydrocarbons, such as LAB and PPO. Fig. ?? shows an image of the orbitals for these π -bonds in a benzene ring: note how the electrons that inhabit these particular orbitals become entirely delocalised.

Because of this delocalised structure, excited atomic π -electrons can stay in what is typically the first-excited state for somewhat longer than typical excited states: lifetimes of $\mathcal{O}(10^{-9}\text{ s})$ as opposed to $\mathcal{O}(10^{-12}\text{ s})$. Moreover, decays from this state can emit light typically in the optical-wavelength range. It is this light emission that is called ‘scintillation light’. Ionised electrons can also recombine — that is, re-enter atomic orbitals — into various excited states, and then decay back to the ground state, also allowing for the possibility of scintillation light to be generated.

The nature of atomic spin selection rules restrict singlet ground-state electrons from exciting into triplet orbitals. However, electrons that were ionised and then recombined have no such restriction, and so are able to enter various excited triplet states. The same selection rules that restrict excitation from singlet into triplet states also works in the other direction, restricting the ability of electrons in excited triplet states from decaying back into the ground state. This does eventually happen, but the lifetimes of these “phosphorescence” decays are typically order of magnitude slower than their singlet-singlet counterparts. As a result, scintillation light typically has, to first order, a ‘fast’ and ‘slow’ time component, which can be seen in Fig. ??.¹

¹In SNO+, we currently model emission of scintillation light from LAB with 3 time components, each roughly one order of magnitude slower than the other.

Fig. 2.4

When using just a single scintillating compound, the very same energy levels that can generate scintillation light are those that can absorb it. This can be a problem for large-scale detectors like SNO+, which depend on scintillation light being unobstructed in its path to the PMTs. Conveniently, this problem can be addressed with the addition of another scintillating component, known (somewhat confusingly) as the primary fluor. In SNO+, this is the PPO added to the LAB.

When an LAB molecule is excited, that energy can be transferred to a PPO molecule through what is known as a ‘non-radiative transfer’. In short, this transfer of energy occurs not through the emission and absorption of optical photons, but through the coupling of the molecules’ electric dipoles.² When the now-excited PPO molecule de-excites to emit scintillation light, the different molecular structure it has generates a different emission spectrum to that of LAB. These longer wavelengths of light are no longer able to be absorbed by the LAB, allowing for a scintillator with less optical absorption.

Adding in one additional component doesn’t have to be the end, either. In SNO+ we plan on adding in the compound BisMSB to the scintillator cocktail. This is a ‘wavelength-shifter’: scintillation light at short wavelengths is absorbed, and then re-emitted at longer wavelengths, where the detection efficiency of the PMTs is greater. More on the properties of the PMTs in SNO+ can be found in Section ???. The net effect of the three scintillating components within SNO+ can be seen in Fig. ???. Note how, as energy is transferred from one scintillation component to another, the wavelength of light emitted gets necessarily longer as energy is lost to heat.

²To be pedantic, photons are still transferred in this energy exchange, but they are virtual instead of real.

The light yield of a scintillator, i.e. the amount of optical photons generated per unit of energy deposited into the scintillator, is a function not just of the scintillator but also the incident particle. In particular, α particles are far more effective at exciting and ionising nearby atoms, and so can deposit far more of its energy into the scintillator per unit volume. However, the strength of this ionisation for α s can actually become at detriment to the generation of scintillation light. Empirically, scintillators follow to first order Birks' Law for their scintillation light yield []: 265
266
267
268
269
270
271

$$\frac{dL}{dx} = S \frac{\frac{dE}{dx}}{1 + k_{\text{Birks}} \frac{dE}{dx}}, \quad (2.1) \quad 272$$

where $\frac{dL}{dx}$ is the number of photons emitted per unit track length, $\frac{dE}{dx}$ is the energy loss of the incident particle per unit track length, S is the scintillator's characteristic light yield constant, and k_{Birks} is the scintillator's "Birks' Constant"³. For minimum-ionising particles such as a 6 MeV electron, the denominator of this equation is close to 1, and so the amount of scintillation light generated is just $\frac{dL}{dx} = S \cdot \frac{dE}{dx}$. However, for α -particles generated in radioactive decays, this denominator can become substantial, and in the limiting case we have merely $\frac{dL}{dx} = S$. In the current phase of SNO+, S and k_{Birks} are measured to be 14,000 γ/MeV and $0.0798 \text{ mm MeV}^{-1}$,⁴ respectively []. 273
274
275
276
277
278
279
280

2.3.2 Optical Processes

Once optical-wavelength photons have been created within the detector, various processes can then occur that can hinder its path towards a PMT, and therefore modify the observed signal. This subsection covers the main optical processes, with a fo- 281
282
283
284

³Birks' Constant is often just written as k_B , but this is easily confused with the far-better known Boltzmann Constant, which is completely different!

⁴This is the Birks' constant used in simulation for α -particles. Other particles, such as electrons, are given slightly different values of k_{Birks} .

cus on Rayleigh scattering, as an understanding of this phenomenon is critical for ²⁸⁵
Chapters ??–??.

Rayleigh Scattering ²⁸⁷

Optical scattering is the general process of how light is scattered by particles within a ²⁸⁸
medium. This is fundamentally an electrodynamical process: an electromagnetic wave ²⁸⁹
is incident on the set of particles within the medium, which induces these particles to ²⁹⁰
oscillate within the field, and therefore generating their own electromagnetic radiation ²⁹¹
in response. Usually, this ‘scattered’ radiation has the same frequency as that of the ²⁹²
incident radiation, and therefore the scattering is said to be *elastic*. It is possible under ²⁹³
certain circumstances for this scattered radiation to be of a longer wavelength than ²⁹⁴
the incident radiation: in which case, energy was absorbed by the particles and so the ²⁹⁵
scattering was *inelastic*. However, this latter type of scattering, also known as Raman ²⁹⁶
scattering, is not relevant for SNO+ [].

The general solution to elastic optical scattering was first described by Gustav ²⁹⁸
Mie [] and Ludvig Lorenz [] in what is now known as *Mie Theory*. In this theory, it is ²⁹⁹
assumed that a plane wave of wavelength λ is incident on a dielectric sphere of radius a . ³⁰⁰
While the general solution to the problem of Mie scattering is somewhat complicated ³⁰¹
(if tractable), in certain regimes one can make further simplifying assumptions that ³⁰²
substantially reduce the complexity of the result. In particular, if one assumes that ³⁰³
the size of the particle is much smaller than the wavelength of light, and that any ³⁰⁴
induced dipole moment can actually be established in the time window allowed by the ³⁰⁵
oscillation period of the electromagnetic field [], then one can obtain *Rayleigh scattering*. ³⁰⁶
This simpler case is so-called because of its initial formulation by Lord Rayleigh []. ³⁰⁷

2.3 Detecting and Recording an Event in SNO+: A Journey

19

One can show that the differential cross-section associated with Rayleigh scattering of unpolarised light off of a single particle, $\frac{d^2\sigma_{\text{Ray}}}{d\theta d\phi}(\theta, \phi)$, is given by []: 308

$$\frac{d^2\sigma_{\text{Ray}}}{d\theta d\phi}(\theta, \phi) = \frac{8\pi a^6}{\lambda^4} \left(\frac{n_{\text{par}}^2 - 1}{n_{\text{par}}^2 + 2} \right)^2 (1 + \cos^2 \theta). \quad (2.2) \quad 310$$

Here, θ and ϕ correspond respectively to the polar and azimuthal angles of the scattered waves, and n_{par} is the refractive index of the scattering particle. Most important to notice about this equation is that the cross-section follows a strong $1/\lambda^4$ dependence, meaning that short wavelengths of light will be scattered to far greater extents than that of longer wavelengths. Secondly, the light is not scattered isotropically, but according to a $1 + \cos^2 \theta$ dependence. This means that most light is either scattered directly forwards or backwards (known as a *backscattering*), and little gets scattered orthogonally to the direction of the incident light. This is useful when it comes to trying to measure scattering in the SNO+ detector, as it provides a handle upon which to distinguish scattered light from isotropically-emitted scintillation light. 320

Of course, we care about the scattering that occurs within an entire bulk medium, not just the scattering off of a single molecule. From a macroscopic perspective, the key quantity of interest is a material's *Rayleigh scattering length*, l_{Ray} : the mean distance a photon is expected to travel before Rayleigh scattering. One can show that, assuming the above differential scattering cross-section, the Rayleigh scattering length is given by []: 321

$$l_{\text{Ray}} = \left[\frac{16\pi}{3} R \right]^{-1}. \quad (2.3) \quad 322$$

R is the *Rayleigh ratio*, $R = \frac{1}{V} \frac{d^2\sigma_{\text{Ray}}(90^\circ)}{d\theta d\phi}$, equivalent to the power of the scattered light per unit volume of the scattering medium per unit incident intensity at $\theta = 90^\circ$. 323

This can lead to a few changes to Rayleigh scattering that are worth noting. Firstly, unlike for a single particle, the electric polarisability of a material can be 330

anisotropic. Anisotropic materials have a modified angular dependence on their 332 differential cross-section, governed by the *depolarisation ratio*, δ . In particular, the 333 $(1 + \cos^2 \theta)$ dependence becomes $(1 + \frac{1-\delta}{1+\delta} \cos^2 \theta)$. For isotropic materials, $\delta = 0$, and 334 so the angular dependence reduces to the original form. 335

Secondly, the above model has been shown to be insufficient to describe liquids 336 or solids [], because of the non-negligible strength of their inter-molecular forces. 337 Fortunately, Einstein [], Smoluchowski [], and Cabannes [] developed a theory for 338 describing how photons can scatter off of the local charge density fluctuations that 339 naturally are present in a medium because of the thermal motion of molecules. The 340 theory shows that the Rayleigh ratio of a medium is related to the medium's dielectric 341 constant, ε , by: 342

$$R = \frac{\pi^2}{2\lambda^4} \left[\rho \left(\frac{\partial \varepsilon}{\partial \rho} \right)_T \right]^2 k_B T \kappa_T \frac{6 + 6\delta}{6 - 7\delta}, \quad (2.4) \quad 343$$

where ρ is the density of the medium, $\left(\frac{\partial \varepsilon}{\partial \rho} \right)_T$ is the partial derivative of the dielectric 344 constant with respect to a changing density assuming a constant temperature T , k_B 345 is the Boltzmann Constant, and κ_T is the medium's isothermal compressibility. This 346 latter quantity is given by the rate of change of volume given a changing pressure of 347 the medium, all at a constant temperature. 348

Furthermore, the Eykman Equation [] has been shown to be an effective empirical 349 formula relating how ε is impacted by density fluctuations to the medium's refractive 350 index, n_{med} : 351

$$\rho \left(\frac{\partial \varepsilon}{\partial \rho} \right)_T = \frac{(n_{\text{med}}^2 - 1)(2n_{\text{med}}^2 + 0.8n_{\text{med}})}{n_{\text{med}}^2 + 0.8n_{\text{med}} + 1}. \quad (2.5) \quad 352$$

This leads to a final formula for the Rayleigh scattering length: 353

$$l_{\text{Ray}} = \left[\frac{8\pi^3}{3\lambda^4} \left(\frac{(n_{\text{med}}^2 - 1)(2n_{\text{med}}^2 + 0.8n_{\text{med}})}{n_{\text{med}}^2 + 0.8n_{\text{med}} + 1} \right)^2 k_B T \kappa_T \frac{6 + 3\delta}{6 - 7\delta} \right]^{-1}. \quad (2.6) \quad 354$$

2.3 Detecting and Recording an Event in SNO+: A Journey

21

Discussions of the scattering lengths currently assumed within SNO+’s optical model for UPW and LABPPO can be found within the theses of Krishanu Majumdar [?] and Esther Turner [?]. In particular, whilst the scattering length of the UPW in the water phase was measured by Esther, major systematics in the measurement remained. Measurements of the scattering lengths in scintillator are the focus of Chapters ??–??.

355

356

357

358

359

Absorption and Re-emission

360

In addition to scattering, an optical medium is also able to absorb light that propagates through it. For a given medium, the *absorption length* l_{abs} is analogous to l_{Ray} described above, and is typically strongly a function of wavelength. For most materials, absorbed light is forever lost, converted into heat. However, for the special case of scintillators, re-emission of absorbed light is possible: this is because of the physics described in Section ??.

361

362

363

364

365

366

367

368

369

Because both scattering and absorption impede a photon’s ability to propagate through a medium directly, it is often possible to measure their combined impact through what is known as the absorption/extinction length, l_{ext} :

$$\frac{1}{l_{\text{ext}}} = \frac{1}{l_{\text{abs}}} + \frac{1}{l_{\text{Ray}}}. \quad (2.7) \quad 370$$

In the water phase, the ‘Laserball’ calibration system was used to measure various optical properties of the detector, including the extinction lengths of the UPW and acrylic as a function of wavelength [?]. Using the water phase scattering measurements made by Esther, Eq. ?? allowed for the estimation of the absorption lengths of these two materials, shown in Figure ?? . Measurements of the extinction length in the scintillator phase is discussed in detail in Chapter ??.

371

372

373

374

375

376

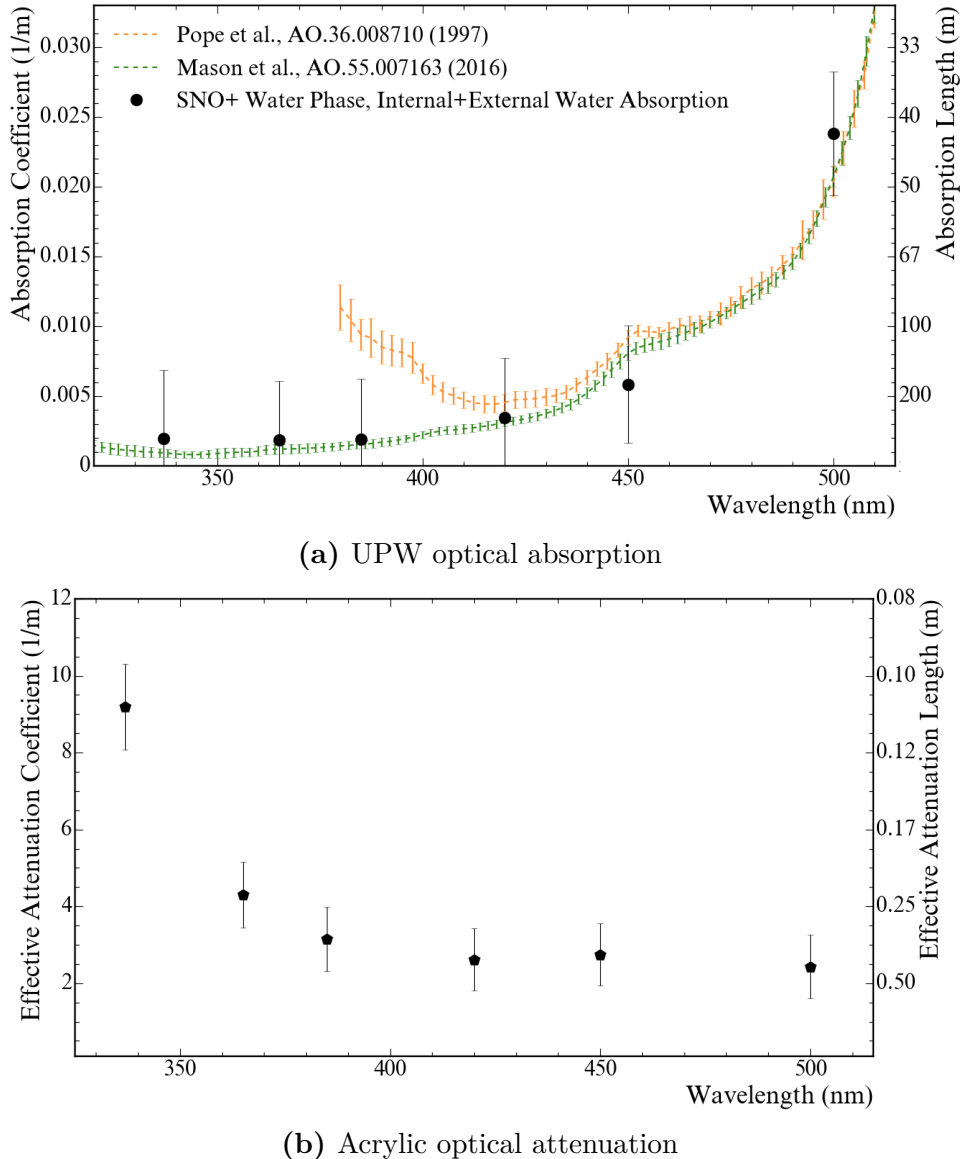


Fig. 2.5: Measured properties of the UPW and acrylic in the water phase, from [?].

Fig. 2.6**Surface reflection and refraction**

377

When light travels through the boundary of one medium to another, both reflection and 378
refraction can be possible, depending on the relative refractive indices of the two media. 379
The refractive indices of the UPW, acrylic, and LABPPO are shown as a function 380
of wavelength in Figure ???. Note that, for most optical wavelengths, LABPPO has 381
a very close refractive index to acrylic, whereas UPW is somewhat farther away. By 382
consequence, negligible refraction is expected in most cases for light travelling between 383
the liquid scintillator and the acrylic; however, substantial refraction is possible for light 384
travelling between acrylic and UPW. Because of this, isotropically-emitting point-like 385
physics events within the AV that are close enough to the acrylic will have some of 386
their light undergo Total Internal Reflection (TIR) at the AV, reflecting back into the 387
AV instead of continuing outward into the outer water. 388

Even when not undergoing TIR, some light at a boundary can still reflect. The 389
fraction of light that reflects is known as the *reflectance* R , compared to that which 390
is able to transmit through the boundary, the *transmittance* $T = 1 - R$. The *Fresnel* 391
Equations determine the reflectance of an interface []: 392

$$R_s = \left| \frac{n_1 \cos \theta_i - n_2 \cos \theta_t}{n_1 \cos \theta_i + n_2 \cos \theta_t} \right|^2, R_p = \left| \frac{n_1 \cos \theta_t - n_2 \cos \theta_i}{n_1 \cos \theta_t + n_2 \cos \theta_i} \right|^2, \quad (2.8) \quad 393$$

where R_s and R_p are the reflectances of *s*- and *p*-polarised light, n_1 and n_2 are the 394
refractive indices of the first and second optical media, and θ_i and θ_t are the angles of 395
incidence and refraction, respectively. For SNO+, we are only interested in unpolarised 396
light, so the total reflectance $R = (R_s + R_p) / 2$. 397

2.3.3 Detection by PMTs

398

- Light gets detected via the PMTs. Note the existence of the PMT concentrators to maximise coverage within the AV, but minimise it in the external water: show the calibrated angular response. 399
400
401
- Remind reader that a PMT converts photons to photoelectrons with a certain quantum efficiency, dependent on the wavelength of light. 402
403
- The process of multiplying the signal induces a spread in the possible generated time of the voltage signal, known as the PMT's transit time spread. 404
405
- The PMT response is also weakly dependent on the number of photoelectrons generated; not enough to be able to confidently distinguish the npe under most circumstances. 406
407
408

[2 pages]

409

2.3.4 Data Acquisition and Triggering

410

- Summarise how a PMT signal becomes digitised via the front-end electronics, briefly. 411
412
- Summarise the triggering system, as I'll have to describe in a later chapter how the SMELLIE hardware fits into this, especially as there have been ongoing SMELLIE triggering issues worth mentioning there! 413
414
415
- Note the information stored by an event: importantly for this thesis, the TAC and QHS per hit, the event's GTID as well as trigger time measured from the 50 MHz clock. The latter is worth mentioning as this is how I determine time differences for my BiPo tagging in the solar analysis. 416
417
418
419

2.4 Calibrations and Detector Modelling**25**

- Finally, note that these get written to file in the ZDAB format.

420

[3 pages]

421

2.3.5 Operation of the Detector

422

- Detector electronics operated through ORCA; allows for different running modes, such as calibrations.
- Mention that data gets split into run and subruns.

423

424

425

[1 page]

426

2.4 Calibrations and Detector Modelling

427

2.4.1 Detector Monitoring

428

- Detector's state is continuously monitored via a number of systems for data quality purposes, including a human detector 'shifter'. This includes the alarm systems for the electronics and slow controls, and 'nearline' monitoring of the detector status.
- CHS and CSS ensure only "good" channels used in any analysis.

429

430

431

432

433

[1 page]

434

2.4.2 Electronic and PMT Calibrations

435

- First main set of calibrations are the ECAs and PCAs. These help us convert raw electronic signal information from PMTs into 'calibrated' hit times and charges. PCAs performed via TELLIE and the Laserball.

436

437

438

- These initial calibrations allow for the first two passes of data processing, resulting in a ‘RATDS’ file format used in optical calibrations. 439
- No need for many details here; this is not a thesis on this topic! 441

[1 page] 442

2.4.3 Energy and Optical Calibrations 443

- After ECAs and PCAs, further calibration is necessary to accurately model the optical properties of the detector. 444
- Describe briefly the function of the Laserball, SMELLIE, and AMELLIE sources in optical calibration (can reference the water-phase optical calibration paper). 446
Details of how each analysis works is obviously not needed here, especially not for SMELLIE as we have 3 chapters to go over that! 447
- AmBe and N16 sources provide further information for calibration 449
- In-situ backgrounds used for more calibration sources, especially for determining the light yield of the scintillator, and Birks’ constant. 451

[2 pages] 453

2.4.4 Event Reconstruction 454

- Once detector is calibrated, event reconstruction becomes possible. Describe main assumption of a SNO+ event: we assume a single-site electron event. 455
- Briefly describe the basics of how energy, position, and time reconstruction works, as this is needed for the solar analysis chapter. Mention existence of direction fitting in scintillator! 457

- ‘Physics’ runs have their events reconstructed in a third pass of data processing, resulting in a ‘fully-processed’ RATDS file as well as a simplified NTUPLE file used in high-level physics analyses (such as my solar analysis). 460
461
462

[2 pages]

463

2.4.5 Event Simulation

464

- Briefly describe overview of RAT software: not only provides the software by which the above data processing occurs, but allows for a GEANT4-based simulation of events in the detector. This simulation includes all parts of the physics described in Section ??, including particle and nuclear physics interactions, optical photon creation and propagation, signal generation and event building based on simulated triggers of the electronics. These simulated events then get processed in the same manner as actual data is. 465
466
467
468
469
470
471

[1 page] [24 PAGES TOTAL]

472

Chapter 3

473

The SMELLIE Calibration System

474

There's a certain Slant of light,

Winter Afternoons —

That oppresses, like the Heft

475

Of Cathedral Tunes —

EMILY DICKINSON

- Basic principle for how SMELLIE works: firing collimated laser light into detector to observe scattering events.
- Analysis will measure and monitor scattering in a detector with changing optics.
- One can try and measure some component of this: the cross-section/scattering length versus wavelength and time, and/or the relative scattering length versus wavelength and time.

476

477

478

479

480

481

[1 page]

482

3.1 The SMELLIE Hardware

483

- Describe the existing hardware, post-upgrade made in Summer 2022. For pre-upgrade hardware, can simply cite previous SMELLIE theses. This includes the path of light into the detector, as well as the path of the trigger signal. 484
485
486
- Make sure to mention explicitly these upgrades: Tony Zummo's fix to the TUBii trigger logic, as well as the addition of the VFA, updated MPU, and modified trigger window. Make sure to motivate why these updates were made. 487
488
489

[7 pages]

490

3.2 Software for SMELLIE Data-taking

491

- Can be brief here! Little has changed since previous theses, so can mostly just summarise and cite. 492
493
- Server running on SNODROP machine, which converts high-level commands into low-level ones that the hardware can interpret. 494
495
- Run plan files written in JSON handed to ORCA which then sends relevant commands to SNODROP which fires as appropriate. 496
497
- Operator interacts with ORCA to perform SMELLIE calibration runs. 498
- After SMELLIE data taken, run description file created, containing metadata about the run conditions, used in analysis. 499
500

[2 pages]

501

3.3 Commissioning SMELLIE in the

502

Scintillator Phase

503

- Explain why commissioning of SMELLIE is needed: Need to confirm that SMELLIE is working as expected; determine intensity "set-points" for different use cases. 504
- Commissioning originally performed by Esther and JeffL back in the water phase; explain why this needed to be re-done for both the scintillator phase and after the hardware upgrades. 505
- No need to describe the Tesseract in detail here - that can be in Jeff L's thesis. But, I do want to show the results of both commissioning campaigns in scintillator-fill, one before the new hardware was added, and one after. 509

[5 pages] [15 PAGES TOTAL]

511

512

513

Chapter 4

514

Simulating SMELLIE Events

515

Max Power : *Kids. From now on there are three ways of doing things: the right way, the wrong way, and the Max Power way.*

Bart Simpson : *Isn't that just the wrong way?*

516

Max Power : *Yes, but faster!*

THE SIMPSONS

Critical to extraction of scattering information from SMELLIE data is an accurate Monte Carlo (MC) simulation of the SMELLIE system. By modelling the laser light emission into the detector correctly, we can simulate how SMELLIE light will be impacted by changing scattering lengths in the detector. Because of the complexity of the optics of the optical fibres used to direct the laser light into the detector, a given SMELLIE event is simulated as a partially-collimated “flash” of visible photons emanating from the emission point of the fibre into the detector. This flash then requires a number of parameters to be correctly described. In particular:

517

518

519

520

521

522

523

524

- **Fibre emission positions** were recorded during the installation of the fibres.

525

- **Wavelength and emission timing distributions** of light pulses were taken from measurements of the laser heads by their manufacturers [], or by colleague Jeff Lidgard in the case of the SuperK wavelength distribution []. 526
527
528
- **The “pulse magnitude”**, defined as the mean number of photons simulated per event, is determined on a subrun-by-subrun basis, and is assumed to fluctuate as a Poisson distribution. 529
530
531
- **The beam profiles**, which describe the angular emission distributions of each fibre, is the focus of this chapter. These are necessary because unlike scintillation light, the light emitted from SMELLIE fibres is not isotropic. 532
533
534
- **Nominal fibre emission directions** attempt to define the centre of the beam for a given fibre. 535
536

This chapter is split into three sections. Improvements to the existing simulation algorithm for the beam profiles are first made, and then the beam profiles themselves are updated. Finally, comparisons between data and simulation are made after the upgrades to investigate any remaining discrepancies. 537
538
539
540

4.1 Improving the SMELLIE Generator Algorithm 541

4.1.1 Previous Attempts at SMELLIE Event Simulation 542

Before we can determine the beam profiles, we must first decide how to specify them. 543
Previous observations show that different fibres can have notably different beam 544
profiles [?], so we let each fibre’s beam profiles be unique. We assume for now that a 545
given fibre’s beam profile is stable over time, and independent of the wavelength of 546
light fired. A straightforward, naïve approach to parameterising a beam profile would 547
be as follows: specify some nominal fibre direction, corresponding to the direction light 548

4.1 Improving the SMELLIE Generator Algorithm

35

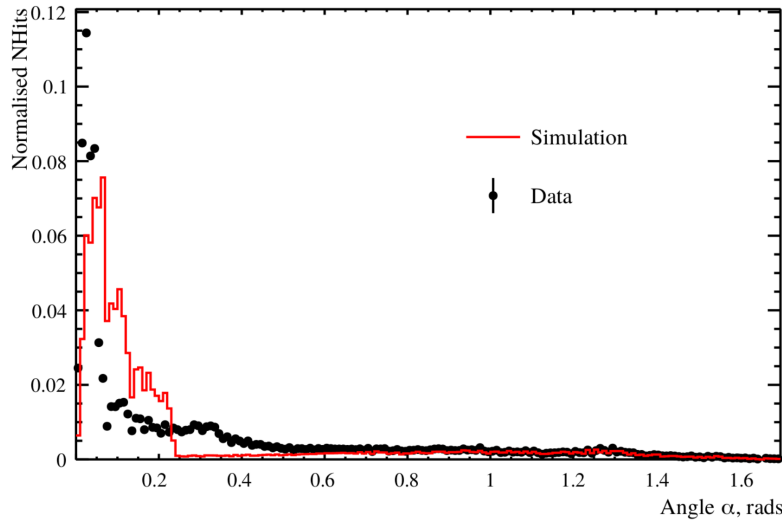


Fig. 4.1: Comparison between a simulation of one of the fibres, made from the 1D beam profile generator (red), with the associated data subrun that was used to create that beam profile (in black). For both MC and data, what is plotted is the PDF of observed PMT hits, as a function of the α angle. Poissonian errors have been added to the data points, but are too small to see. Clearly, this 1D generator does not replicate the observed beam profile correctly. Figure taken from [?].

takes travelling from the fibre to the centre of the “beamspot” observed on the other 549 side of the detector. Then, specify a 1D beam profile, corresponding to the probability 550 density of firing a photon at a given polar angle α relative to the nominal direction. 551 One might even assume this distribution is Gaussian. The distribution in azimuthal 552 direction, ϕ , is assumed to be uniform. 553

This 1D beam profile approach was used initially for SMELLIE, and remains in 554 use for the other ELLIE sub-systems within SNO+. However, when SMELLIE data 555 was taken in the water-phase of the experiment, simulations using these beam profiles 556 failed to match them well at all - see figure ?? for an example. Not only was the 557 distribution in α not Gaussian, a distinct speckle-pattern can be observed within the 558 beamspot that is not uniform in ϕ . This fact led to colleague Esther Turner building a 559 SMELLIE generator that could handle 2D beam profiles: dependent on both α and ϕ . 560 The distribution was stored as a map from each inward-pointing PMT in the detector 561

to a relative intensity value. This was chosen because the beam profile shapes were 562
calibrated from existing SMELLIE data — more on this in section ??.

This original 2D generator then sampled the beam profile via a rejection sampling 564
approach, outlined as follows:

1. Propose a test direction (α, ϕ) , by generating ϕ uniformly in the interval $[0, 2\pi]$, 566
and α according to some pre-determined Gaussian distribution, known as the 567
Gaussian envelope. 568
2. Given this test direction, calculate where a line following this direction from the 569
fibre of interest will hit the PSUP on the other side of the detector. Find the 3 570
closest PMTs to that point. 571
3. From those PMTs, obtain their relative intensity values from the beam profile 572
mapping, and perform an interpolation based on how close each PMT is to the 573
PSUP intersection point. This gives an interpolated relative intensity value for 574
this test direction. 575
4. Because we are sampling using the angular coordinates (α, ϕ) , differential area 576
elements over this space of directions do not have the same size. We can correct 577
for this fact by multiplying our interpolated relative intensity by $\sin \alpha$, which 578
corresponds to the Jacobian of the direction-space. 579
5. Calculate the value for the Gaussian envelope along this test direction. 580
6. Throw a random number uniformly between 0 and the Gaussian envelope value. If 581
the random number is less than the interpolated intensity, then this test direction 582
is accepted, and a photon is generated with that direction. Otherwise, we reject 583
the direction and try the whole process again. 584

4.1 Improving the SMELLIE Generator Algorithm

37

This generator certainly works, but has a key problem: efficiency. The 1D generator was able to generate a SMELLIE event (that is, to fully specify the starting parameters of all the photons emitted from a fibre) at a speed of ~ 1 ms. However, the 2D generator specified here could take upwards of ~ 50 s *per event* to generate. Because a typical SMELLIE analysis requires simulating many millions of events, the CPU time taken to perform this quickly became unfeasible. Fixing this generator speed problem was a high priority for the SMELLIE analysis.

585

586

587

588

589

590

591

4.1.2 The new generator

592

On careful inspection of the existing 2D generator, the main reason for the slowness of the algorithm is the use of a rejection approach. Even with use of the Gaussian envelope, which was included to help with speed, the vast majority of proposed directions are never selected. Figure ?? shows a histogram of number of attempts per event it took for a valid direction to be chosen for a representative SMELLIE simulation. Moreover, the calculations needing to be done for every proposed direction are relatively complex, notably trying to find the 3 nearest PMTs to some point on the PSUP.

593

594

595

596

597

598

599

A new 2D generator was built with these thoughts in mind. Firstly, the rejection method would no longer be used, given its inefficiency. We would also endeavour to try and “pre-calculate” as much as possible before run-time. Starting with the existing PMT relative intensity maps, we plot these in the 2D direction-space ($1 - \cos \alpha, \phi$): see Figure ???. In a toy-MC simulation, 500,000 directions are then thrown uniformly in this 2D space per fibre. For each direction, the same method of obtaining an interpolated intensity value from the nearest PMTs to the corresponding point on the PSUP as from the original 2D generator was performed, the only difference being that these calculations were done well before any actual SMELLIE simulation. Figure ?? shows the interpolated intensities obtained for one fibre.

600

601

602

603

604

605

606

607

608

609

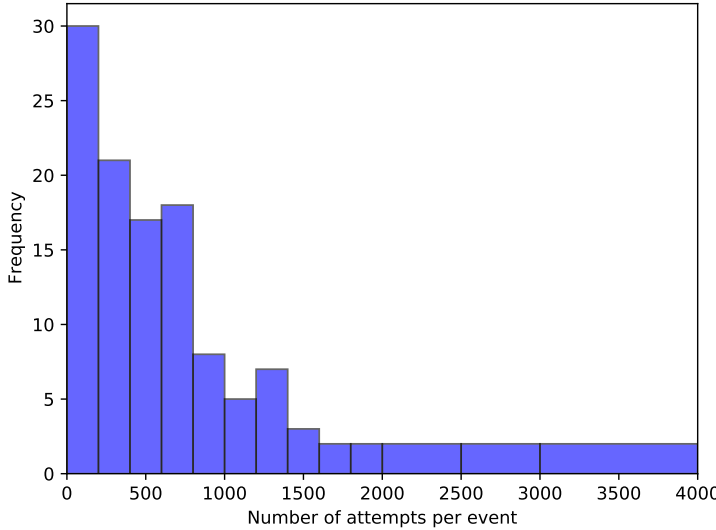


Fig. 4.2: Typical distribution of the number of attempts it takes for the existing 2D generator before the test direction gets accepted, per event.

Following this, the sampled intensities were then binned into a 2D histogram, where 610
the bin value corresponds to the sum of all intensities for all directions found within this 611
bin. Choosing a sensible binning procedure is important: too few bins, and necessary 612
information about the shape of the beam is lost, whilst too many bins can oversample 613
the data and capture statistical artefacts in the sampling process instead of just the 614
beam profile. As a balance, 15 bins were chosen along the ϕ direction, and 60 in 615
 $r = 1 - \cos \alpha$. This was chosen to ensure that a reasonable number of PMTs were 616
located within each bin, lessening the impact of any statistical fluctuations. Although 617
the bins in ϕ were chosen to have uniform width, this was decided to be not the 618
case for the other axis, as there is far more important information near $r = 0$ (the 619
beamspot). Instead, the width of the bins in r were calculated so that roughly the 620
same total probability was contained in each r -strip. By consequence, bins near the 621
beamspot typically are of significantly smaller size than ones much further out. This 622
allows us to both capture any rapid changes in intensity near the beamspot, where this 623

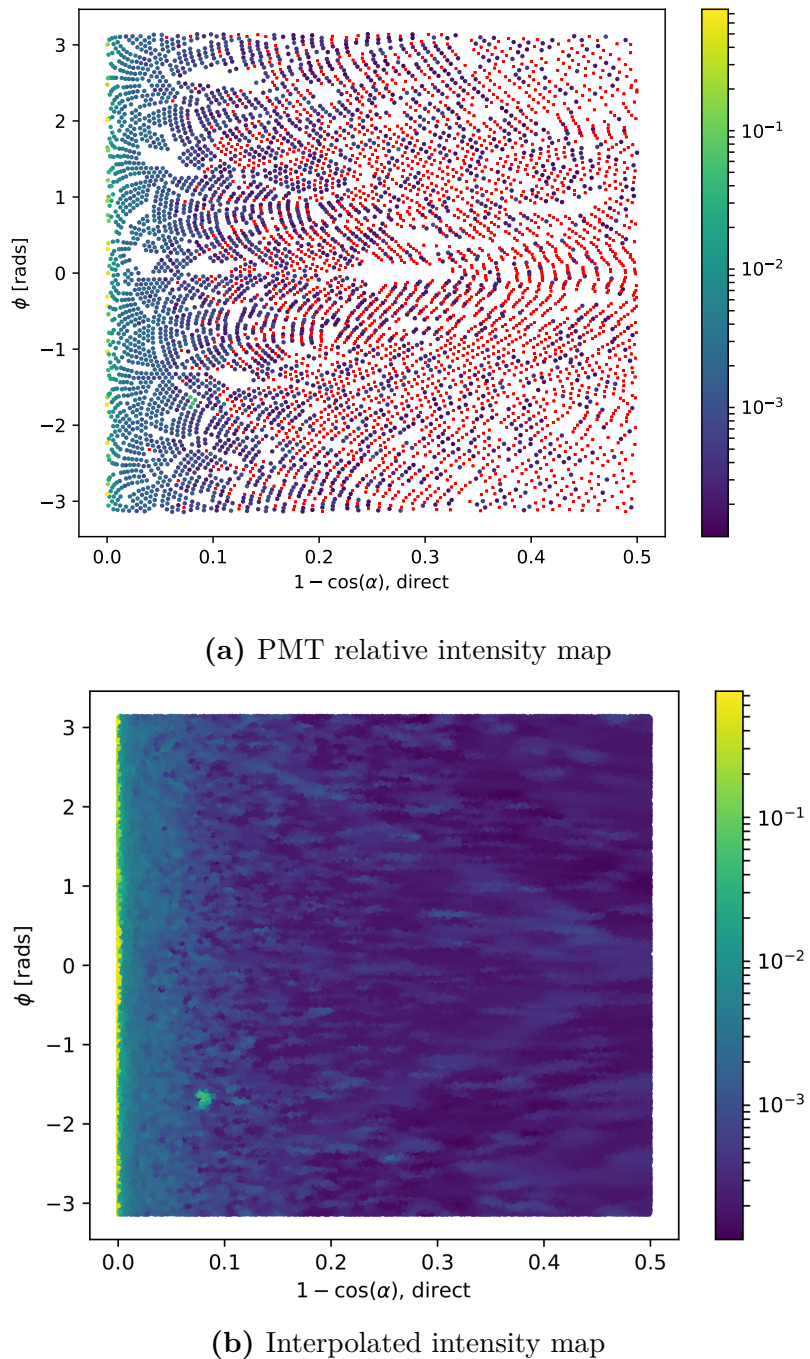


Fig. 4.3: The first step in the new method for preparing the new generator. In (a), the relative intensities used for the existing beam profile of fibre labelled FS055 are shown for each PMT, the position on the plot indicating the location of that PMT in the fibre coordinates. The colour indicates the relative intensity; PMTs marked red have an intensity of zero. Figure (b) shows the result of throwing 500,000 directions uniformly over this 2D space, the intensity of each point given by interpolating the intensities of nearby PMTs.

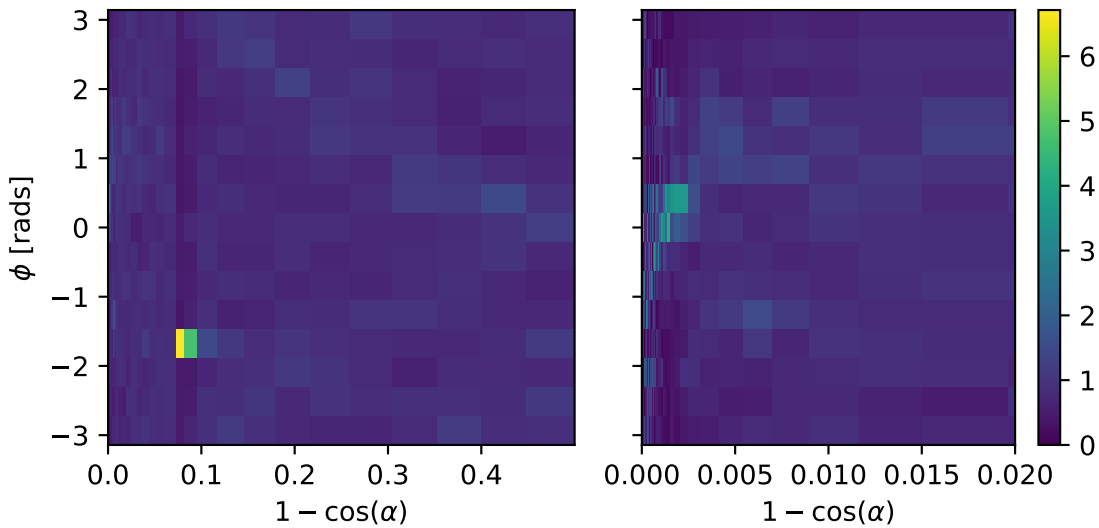


Fig. 4.4: Histogram of interpolated intensities within the 2D direction-space. The left view shows the full histogram; the right is a zoomed-in version near the beamspot. Unlike the binning in ϕ , the bin widths in r are not at all uniform. Instead, they have been determined such that the area summed over a given “strip” of bins of constant r will be the same.

matters greatly, and smooth out the very-low intensities seen at larger polar angles. 624
One of these histograms can be seen in Figure ??: the large change in bin widths as a 625
function of r is clear. One can also see that near the beamspot notable dependence on 626
the intensity as a function of ϕ . The mysterious “spot” at $r = 0.08$, well out of the 627
beamspot, is an indication that the underlying beam profile data being used requires 628
improvement: more on this in section ??.

The Cumulative Density Function (CDF) of this intensity histogram as a function 630
of bin was then produced, where the bins were ordered through a raster-scan: scanning 631
first over ϕ , and then r . The CDF was then normalised to 1 so that it was well-defined. 632
It is this CDF object that is then loaded in and sampled from during event generation. 633
To do this, an “inverse-CDF” approach was used, which has the major benefit over 634
rejection sampling of always producing a valid direction for every sample made. The 635
algorithm works as follows:

1. Throw a random number uniformly in $[0, 1]$.

637

4.2 Improving the beam profiles**41**

2. Perform a binary search to find the bin that has the largest CDF value below this random number. 638
3. Look at the bin edges in ϕ of this selected bin: use linear interpolation of the random number to obtain a ϕ value located between these two ϕ -values. 640
- 641
4. Look at the selected bin's r -bin edges, and select a value of r by throwing a second random number uniformly between the two edges. Convert this r into a polar angle α . 642
- 643
- 644
5. The photon's direction is defined by the (α, ϕ) chosen by this process. 645

Because of the relative simplicity of this algorithm compared to the previous 2D generator, the speed improvement was very large: generation now took ~ 1 ms per SMELLIE event, a speed improvement of nearly 50,000. Event generation became as fast as it was when the 1D generator was being used. Furthermore, because of the approach taken, this major speed improvement comes at no sacrifice in accuracy. 646

647

648

Figure ?? shows a comparison of the average number of photoelectrons (npe) per event per PMT between water-phase SMELLIE data and simulations with both the old and new 2D generator. One can see clearly that both generators are as accurate as one another. Note that this plot uses the updated beam profiles as explained in the next section. 649

650

651

652

653

654

655

4.2 Improving the beam profiles

656

Even with the new 2D profile generator, a problem remains: the simulation fails to reasonably recreate data, and much of this appears to be because of the poor beam profile data being used. The curious “spot” for one of the fibres was already noted in the previous section that doesn't seem to be physical, and more broadly at large angles 657

658

659

660

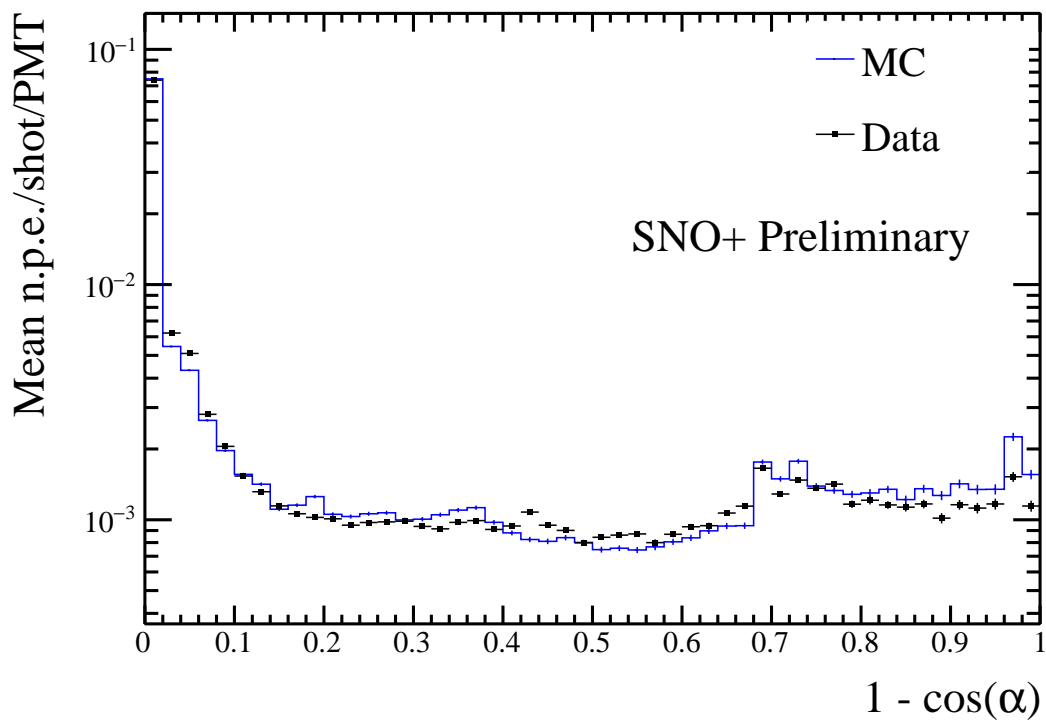


Fig. 4.5: Comparison of water-phase data to MC generated using both the old and new 2D beam profile generator approaches, with the updated beam profiles. Both versions of the generator are consistent with one another, but the new generator is many times faster.

4.2 Improving the beam profiles

43

for all the fibres there are large swathes of PMTs with an intensity of zero, providing
 little useful information about the beam shape. It was shown in [?] that with the
 old 2D generator, the systematic uncertainty on the beam profiles was the dominant
 source of error in the main SMELLIE analysis. To help improve this situation, it was
 decided to update the existing beam profiles.

These old beam profiles were originally determined by looking at SMELLIE data
 taken during the water-phase. Specifically, a “medium”-intensity subrun with one
 of the lasers firing at a wavelength of 495 nm, was chosen for each fibre. “Medium”-
 intensity corresponds to firing the relevant laser at a set intensity determined during
 an earlier commissioning process, for which the maximum occupancy of PMT hits at
 that intensity, i.e. the proportion of hits per event, corresponded to roughly 80%. This
 value was chosen as it allowed for high statistics in a relatively short run-time, but not
 so intense that the occupancy of any given PMT in the beamspot was 100%. Because
 Rayleigh scattering is strongly-dependent on wavelength, the long wavelength of light
 was chosen so that impacts from this scattering were small in the data.

SNO+ PMTs are unable to distinguish the exact number of photoelectrons being
 generated. One is typically only able to know if a PMT has been triggered at all, by
 any number of photoelectrons. As a result, the occupancy of a PMT over a number
 of SMELLIE events, o , is a biased estimator of the mean number of photoelectrons
 generated, μ . Assuming the number of photoelectrons generated in a given event
 follows Poisson statistics, the probability of generating k photoelectrons is:

$$P(k|\mu) = \frac{\mu^k e^{-\mu}}{k!}. \quad (4.1)$$

The probability of observing a “hit” in a given PMT corresponds to generating at
 least one photoelectron:

$$P(\text{hit}|\mu) = P(k \geq 1|\mu) = 1 - P(k = 0|\mu) = 1 - e^{-\mu}, \quad (4.2) \quad 685$$

which implies after rearrangement that one can determine the mean number of photo-electrons per event from the occupancy by: 686
687

$$\mu = \ln(1 - o). \quad (4.3) \quad 688$$

This is the reason why we want to avoid PMTs with occupancies of 100%: they preclude one's ability to convert into a value for μ by looking at occupancy alone. We call this conversion from occupancy into npe the “multi-hit correction”. The impact of this correction is typically small for most PMTs, but can become very significant in a fibre's beamspot. 689
690
691
692
693

Once the npe mapping from data was obtained, a correction was then made for the detector's optics: even ignoring a fibre's beam profile, we still expect certain PMTs to be illuminated more than others because of e.g. reflections off the AV, or the solid angle subtended by the PMT bucket opening. For each fibre, a simulation was made where the beam profile was set as isotropic, and the corresponding npe mapping obtained: this map held information about the detector optics only. The beam profile mapping was then derived by simply dividing each fibre's npe mapping from data to its associated isotropic MC npe map. It is these maps that were first used in section ???. 694
695
696
697
698
699
700
701

4.2.1 Combining beam profile datasets

702

Fortunately, much more SMELLIE data was taken during the water-phase than was used for the original beam-profiling analysis. This additional data can be combined with that which was already used to far better constrain the beam profiles. In particular, given the existing assumption that scattering effects are minimal above wavelengths of 703
704
705
706

4.2 Improving the beam profiles

45

Run Number	Run Type	Comments
114,018	All PQ lasers; SuperK laser in 400–500 nm range	Only PQ495 laser and SuperK at 495 nm is used
114,023	SuperK laser in 500–600 nm range	Part 1 of this wavelength range; crash occurred on last subrun, so that subrun is ignored
114,034	SuperK laser in 500–600 nm range	Part 2 of this wavelength range

Table 4.1: Water-phase runs used for new beam profiling.

~490 nm, all data taken with wavelengths above this can also be used. The specific runs (and associated comments about their specifics) are described in Table ???. Because high-intensity runs require a different analysis approach (PMTs with high occupancies must use charge, not occupancy, to estimate npe), for this analysis we only considered subruns that used low or medium intensity set-points.

For each subrun j of data per fibre, we look only at PMT hits for each PMT i that has been identified as “good” for that subrun¹, $i \in G_j$. G_j here represents the set of good PMTs in subrun j . In particular, a “good” PMT must have valid electronic and timing calibrations, be at high voltage and masked into the detector’s trigger system for that subrun. In addition, an angular cut of $\alpha < 60^\circ$ was made to remove PMTs that are well outside any reasonable beam direction. To isolates the hits arriving directly from the fibre without reflecting, scattering, or being noise, a time cut was also made. Because what matters is the time relative to emission from the fibre, and the expected time-of-flight from fibre to different PMTs varies, a quantity known as the time residual was used. Starting with the calibrated hit time of a given PMT relative to the event’s trigger time, t_{hit} , the expected time-of-flight t_{TOF} from the fibre to the PMT was subtracted, estimated with the collaboration’s “Light Path Calculator”. Then, the emission time was also subtracted, t_{emm} , estimated by looking at the second-earliest value of $t_{hit} - t_{TOF}$ within the fibre’s central beamspot, defined as the PMTs for which

¹Strictly speaking, a PMT’s “goodness” is only determined on a run-by-run, not a subrun-by-subrun level, but this has no impact on the analysis.

$\alpha < 3^\circ$. It was found that a “loose” time residual cut of $t_{res} \in [-10, +12]\text{ns}$ was sufficient to remove the vast majority of non-direct light with little signal sacrifice. In the situation where a subrun with intensity was very small, it would not regularly have at least two hits in the beamspot, and so the time residuals calculated would not be valid for many events. To avoid this situation, a cut was made on any subruns with mean intensities below 9 within their beamspot. This value was chosen as it would mean a 2σ fluctuation downwards of $2 \cdot \sqrt{9} = 2 \cdot 3 = 6$ npe would still have more than the 2 hits necessary for timing reconstruction. One fibre, FS207, has no data subruns that satisfy this condition, and as such will have to be dealt with separately. For the time being, this fibre was ignored.

Extracting the underlying beam profiles from these data required some careful thought, especially because different subruns could have different intensities. Considering a PMT i in subrun j , the mean number of photoelectrons generated per event in that PMT for that subrun, μ_{ij} can be decomposed as follows:

$$\mu_{ij} = I_j k_i = I_j b_i f_i. \quad (4.4) \quad 740$$

I_j is the intensity of the subrun, i.e. the mean number of photons generated from the fibre in that subrun per event. k_i is the probability that a given photon generated at the fibre source ends up generating a photoelectron in PMT i . This itself can be further split into two components: b_i , the probability that a given photon at the fibre source points in the direction of PMT i ; and f_i , the probability that a given correctly-pointed photon actually makes it to the PMT and successfully generates a photoelectron. It is b_i that is the actual beam profile we would like to measure.

Letting p_{ij} be the probability of observing a hit for a given event on a given PMT, the probability of observing m_{ij} hits out of N_j events in the subrun will be

 4.2 Improving the beam profiles

binomially-distributed:

750

$$P(m_{ij}|\mu_{ij}) = L(\mu_{ij}|m_{ij}) = \binom{N_j}{m_{ij}} p_{ij}^{m_{ij}} (1-p_{ij})^{N_j-m_{ij}} = \binom{N_j}{m_{ij}} (1-e^{-\mu_{ij}})^{m_{ij}} e^{-\mu_{ij}(N_j-m_{ij})}. \quad (4.5)$$

751

Here we have used equation ??, and noted that this probability distribution in m can be re-framed as a likelihood function for the parameter μ_{ij} . Considering only a single subrun of data, the maximum likelihood estimate of the parameter μ_{ij} can be shown to be:

752
753
754
755

$$\langle \mu_{ij} \rangle = -\ln \left(1 - \frac{m_{ij}}{N_j} \right) = \ln (1 - o_{ij}) \quad (m_{ij} \neq N_j), \quad (4.6)$$

756

where o_{ij} is just the occupancy of PMT i in subrun j . This is just the multi-hit correction formula seen in equation ??, which makes sense.

757
758

When looking at multiple subruns for the same fibre, the total likelihood function for a given PMT when considering all the data for a given fibre will be the product of the likelihoods from each dataset,

759
760
761

$$L(\{I_j\}, k_i | \{m_{ij}\}) = \prod_j L(I_j, k_i | m_{ij}) = \prod_j \binom{N_j}{m_{ij}} (1 - e^{-I_j k_i})^{m_{ij}} e^{-I_j k_i (N_j - m_{ij})}. \quad (4.7)$$

762

This leads to a log-likelihood distribution of

763

$$\mathcal{L}(\{I_j\}, k_i | \{m_{ij}\}) = \sum_j \left[\ln \left(\binom{N_j}{m_{ij}} C_{m_{ij}} \right) + m_{ij} \ln \left(1 - e^{-I_j k_i} \right) - I_j k_i (N_j - m_{ij}) \right]. \quad (4.8)$$

764

Formally, one could combine the likelihoods of all the PMTs together, and by looking at the maximum likelihood estimates for each of the parameters measure the parameter values this way. However, the set of equations one obtains through this approach quickly become analytically intractable, because the PMTs are coupled by the intensity values I_j . Even a direct numerical approach would be liable to fail: for a given fibre

765
766
767
768
769

there can be dozens of subruns, and many thousands of PMTs of relevance, so the
 dimensionality of the system of equations would be far too large. 770
 771

Because of this, a different approach was taken. It is expected that in a subrun the
 total npe, summed over all good PMTs, should be proportional to the intensity value
 I_j . One must be careful about this construction — different subruns can have different
 sets of good PMTs, so two subruns with identical I_j values could have a larger summed
 npe merely because more PMTs were good in that subrun. To counter-act this effect,
 only PMTs that were classified as good in *all* subruns being analysed for that fibre
 would be used for the npe summation. In other words, we use data from PMT i for
 summing only if: 779
 780

$$i \in \mathcal{I} = \bigcap_j G_j. \quad (4.9)$$

We can then define the summed npe for a given subrun as $S_j = \sum_{i \in \mathcal{I}} \text{npe}_{ij}$, and assert
 that $I_j = cS_j$. By finding a value proportional to I_j , there is now enough information
 to maximise the log-likelihood $\mathcal{L}(k_i | \{m_{ij}\}, \{I_j\})$ with respect to k_i for each PMT
 independently, and hence obtain estimates for these k_i parameters. 784
 781
 782
 783

Of course, what is actually wanted are the underlying b_i values, not k_i . This is
 where isotropic simulations come in. For each run of data used, a matching isotropic
 MC was produced. As an example, a simulation for run 114,023 contained 200,000
 events for each fibre using an isotropic beam profile, over the full wavelength range
 considered in this run, 500–600 nm, using the same run conditions as in data (which
 PMTs were at high voltage, etc.). 790
 785
 786
 787
 788
 789

For each isotropic MC run, both I_j^{MC} and k_i^{MC} were calculated via the method
 described above. Because the simulations were isotropic, the underlying value for b_i
 was constant across all the PMTs, and so $a k_i^{MC} = f_i$. By doing some rearranging of
 791
 792
 793

4.2 Improving the beam profiles

49

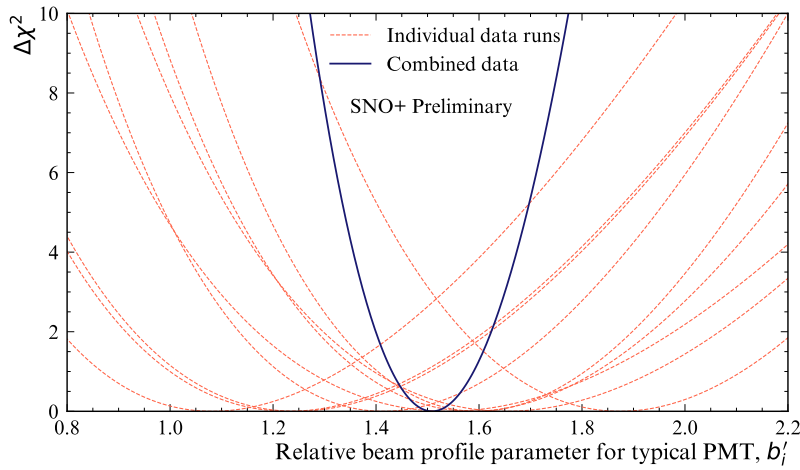


Fig. 4.6: Plot of $\Delta\chi^2 \simeq X_i$, twice the negative log-likelihood ratio, for both single subruns of a typical PMT, and when all relevant subruns are combined.

equation ??, we find that:

794

$$\mu_{ij} = I_j b_i f_i = c S_j b_i a k_i^{MC} = (acb_i) S_j k_i^{MC}. \quad (4.10) \quad 795$$

As a result of this, given the set $\{S_j\}$ and k_i^{MC} , one can maximise the log-likelihood \mathcal{L} 796 with respect to $b'_i = acb_i$ numerically, to obtain the maximum likelihood estimate of b'_i . 797 Because a and c were global constants of proportionality, they would become irrelevant 798 as soon as the beam profile was normalised in the CDF-creation process outlined in ???. 799

Figure ?? shows the shape of this log-likelihood distribution for a particular PMT 800 when considering fibre FS007's beam profile. One can see how individual subruns 801 provide much more information when combined than if one looked at a single subrun 802 alone. 803

Another benefit of using this log-likelihood approach is that the resulting distribution's shape can be used for uncertainty estimation. In almost all cases, Wilks Theorem [?] allows us to produce 1σ confidence intervals about the maximum

likelihood estimate for b'_i , $\langle b'_i \rangle$, because

$$X(b'_i) = -2 [\mathcal{L}(b'_i) - \mathcal{L}(\langle b'_i \rangle)]$$

approximates a χ^2 -distribution. As a result, the error bounds on our parameter estimate 804
are given by when $X = 1$. The fact that the shape of X can be well-approximated by 805
a quadratic in the region near $X = 0$ indicates the validity of Wilks' Theorem being 806
used here. 807

Only a couple of exceptions to this approach of parameter estimation are possible. 808
In the case where $m_{ij} = N_j$, i.e. a PMT has 100% occupancy, no maximum likelihood 809
estimate exists: we need not worry about this, as subruns where this occurs have not 810
been used. On the other end, however, there are some PMTs for certain fibres where 811
after all subruns of data have been included, there remains no hits. In this scenario, 812
one can show that the log-likelihood becomes linear in the beam profile parameter: 813

$$\mathcal{L}(b'_i | \{m_{ij} = 0\}) = b'_i k_i^{MC} \cdot \sum_j [I_j N_j]. \quad (4.11) \quad 814$$

This scenario is very much reminiscent of rare-decay searches, and a similar approach 815
can be used. A 1σ upper limit on the possible value for b'_i can be analytically-calculated 816
to be: 817

$$b'_{i,ulim} = -\frac{k_i^{MC} \sum_j [I_j N_j]}{\ln [1 - \text{erf}(1/\sqrt{2})]}, \quad (4.12) \quad 818$$

where $\text{erf}(x)$ is the error function. [18 pages for above two sections] 819

4.2.2 Results & Discussion

WARNING: contents of this subsection will be gutted, focusing merely on impact of 821
combining data sets. Details about discrepancies will be covered in the next section. 822

4.2 Improving the beam profiles

51

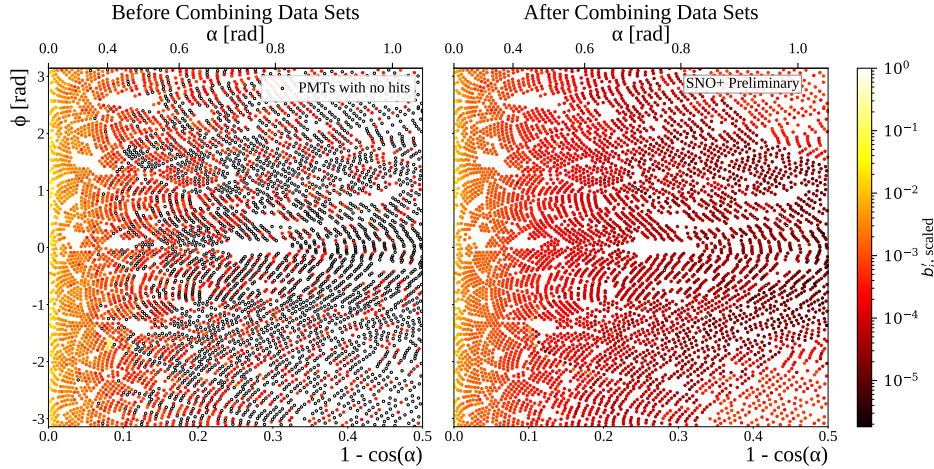


Fig. 4.7: Comparison between old and updated beam profiles for fibre FS055, after combining multiple data sets. Once again, the relative intensities (b'_i) for each PMT are given by the colour of each point, the position of each plotted in the 2D (r, ϕ) -space. The relative intensities have been both scaled here so that the largest value equals 1. Hollowed-out points are PMTs that, even after all relevant subruns have been combined, have no PMT hits.

[Will just be 1 page] Figure ?? shows the impact of using additional subruns of data 823 on a typical beam profile. One can clearly see the great reduction in the number of 824 PMTs with no hits in data. That many more data sets were included allowed for the 825 major increase in dynamic range available for measuring these b'_i values. One can also 826 note that by including additional data the curious spot that was seen in the old beam 827 profile our at $r \approx 0.08$ has gone, further indicating that it was an artefact of that single 828 data set. 829

Further details can be gathered from the interpolated intensity maps, one of which 830 can be seen in figure ?? . There are two curious stand-out features that can be seen here: 831 firstly, there are multiple distinct parabolic arcs. These correspond to the shadows of 832 the ropes that hold up/down the AV. More precisely, they are the mismodelling of 833 those shadows — if the shadows were in the right place in the isotropic MC, then they 834 would correctly cancel out any decreased intensity seen in the data of shadowed PMTs. 835 These shadows could be mismodelled either because the positions of the ropes in the 836 MC are in the wrong place, or the fibre's emission position is wrong. Note that any 837

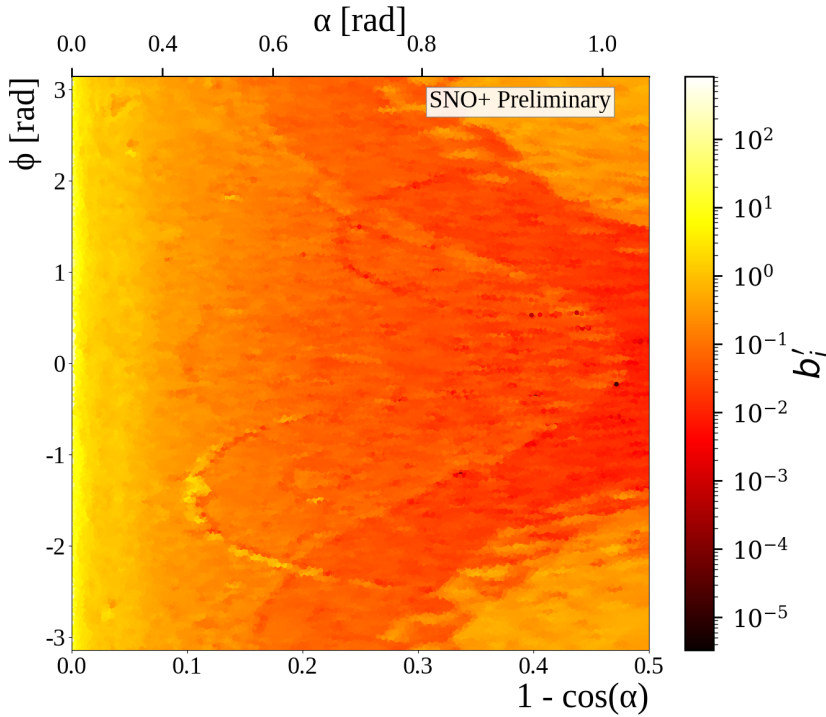


Fig. 4.8: Interpolated intensity map for the new updated beam profile of fibre FS055. The misalignment of rope shadows and AV effects, can both be seen.

mismodelling of the fibre's nominal emission direction has no impact on this shadowing 838 problem, as changing that direction merely causes a change of basis in the (r, ϕ) -space. 839 The latter possibility of incorrect fibre positions are more likely, and in fact these arcs 840 in the beam profiles could be used as an effective way to correct for this problem. 841

The second distinctive feature of this intensity map is the large band of lower 842 intensity varying between $r \approx 0.2 - 0.5$, followed by larger intensity out at large 843 r values. This feature comes from light reflecting off the AV surface, or internally- 844 reflecting. The reason for this band's functional dependence on ϕ is that this particular 845 fibre, FS055, has a nominal fibre direction $\sim 10^\circ$ from pointing radially-towards the 846 detector's centre. This feature appears in the updated beam profiles of all fibres, but 847 its shape depends on the particular fibre's direction — for fibres pointing directly 848 towards the detector's centre, there is little ϕ -dependence observed. Like the ropes, 849

4.2 Improving the beam profiles**53**

this feature must come from some form of mismodelling of the optics of the AV. A de-facto shadowing of PMTs in line with tangents from the AV surface which intersect the fibre position is to be expected. One also expects PMTs at polar angles larger than this to have their observed intensities boosted from reflected light off the AV. However, the discontinuities seen in the beam profiles indicate that for whatever reason this effect has been over-emphasised in the simulation. 855

There is a further phenomenon that can be seen, by comparing beam profile values obtained from a single subrun to the updated combined beam profile. This can be done by calculating the residuals corresponding to the single subrun, relative to the combined data set. The residual is negative if the combined data sets have a b'_i below the equivalent for a given single subrun; that is, the combined model underestimates this subrun for that PMT. 861

This information was plotted for two different subruns from the same fibre, seen in figure ???. One subrun was the same one used by Esther Turner for the original 2D beam profiling, with a wavelength of 495 nm; the latter was at the longer wavelength of 595 nm. For both subruns, most PMTs are seen to have intensities well-modelled by the combined model. However, there appears to be a significant amount of mismodelling within the beamspot. There also appears to be some systematic shift between data and model at somewhat larger polar angles. Moreover, this mismodelling seems not to be merely random, but a function of wavelength: at shorter wavelengths the beamspot tends towards being overestimated and then underestimated at larger values of α . At longer wavelengths, the beamspot becomes underestimated, with larger angles getting overestimated. This indicates that there appears to be a wavelength-dependence on the beam profiles, contradicting one of the main assumptions which we used to combine the water-phase data in the first place! All three of these features — rope shadows, AV reflections, and wavelength dependence — add systematic uncertainty to the beam 875

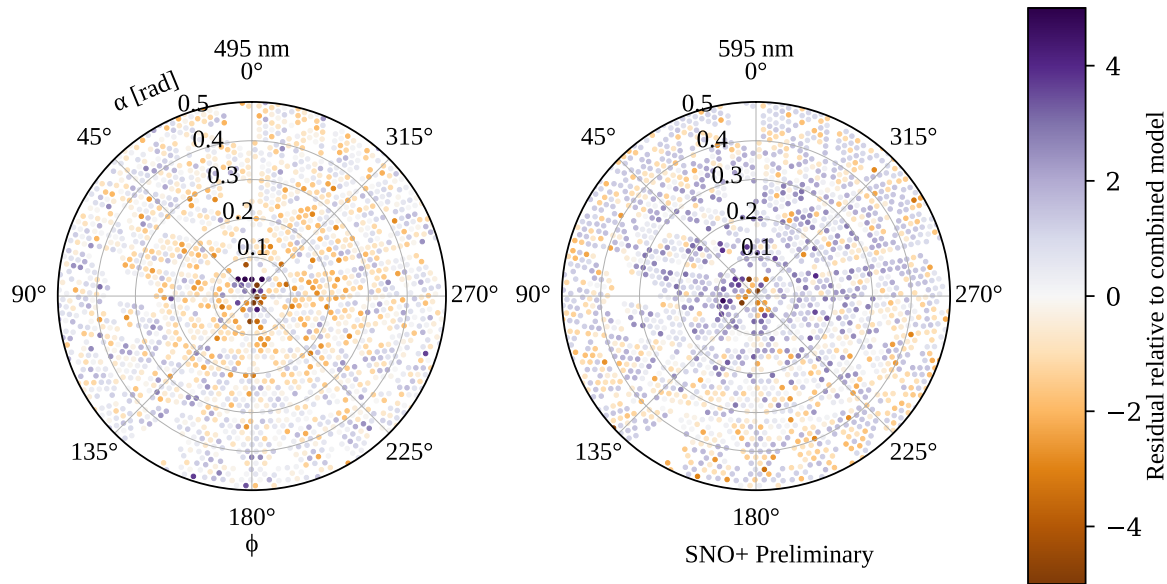


Fig. 4.9: Residuals from subruns at two different wavelengths, both compared to the combined beam profile model for fibre FS055. A negative sign, and hence bluer colours, indicate that the combined model underestimates the observed intensity for that particular subrun. Values with a magnitude beyond 5 are shown capped at this maximal value for the purposes of this plot. These PMTs are plotted in the polar fibre coordinates (α, ϕ) .

profiles, beyond the statistical uncertainty as measured by the width of the likelihood 876
distribution. Certainly if one wanted to further improve the uncertainties in the beam 877
profiles, tackling these challenges would be key. 878

4.3 Comparisons between Data and Simulation

- This focuses on disagreements noticed between data and MC even after the new 880
generator and beam profiles have been used. 881
- Important to mention that none of these are necessarily game-ending, they are 882
just systematics that may or may not be substantial in a given analysis with 883
SMELLIE.. 884

4.3 Comparisons between Data and Simulation

55

4.3.1 Forward Hemisphere Discrepancies

885

- The continued disagreement between data and MC when it comes to measured npe in various parts of the “forward” hemisphere. This includes:
 - The central beamspot, 888
 - The TIR region, 889
 - Rope shadows, 890
 - A noticeable wavelength-dependence. 891
- This is pretty much most of the contents of Section ???. 892

[4 pages]

893

4.3.2 Emission Time Discrepancies

894

- For certain lasers, a strong mismatch in the observed hit time residuals for prompt light. 895
- A mysterious +18 ns bump seen for the PQ495 laser. 897
- A trigger jitter in the SuperK laser. 898

[3 pages]

899

4.3.3 Backward Hemisphere Discrepancies

900

- The observed distribution of hits vs time and angle in MC does not match data in a number of ways for PMTs near the fibre emission point. 901
- Includes the outer-water scattering length, rope reflections, and investigations into whether certain modifications to the optics could plausibly fix things (so far, no). 903

905

Chapter 5

908

Analysis of SMELLIE Data in the Scintillator Phase

909

910

This chapter contains two sets of analyses: measurements of the extinction lengths 911
of the scintillator as a function of wavelength and time, as well as monitoring the 912
Rayleigh scattering length over time. 913

5.1 Extinction Length Analysis

914

5.1.1 Motivation

915

- Explain motivating observations for this analysis: a substantial discrepancy 916
between MC and data seen in the radial profiles of nhitsCleaned for ^{210}Po after 917
the PPO top-up campaign. Performed by Serena. 918
- Hypothesis of a shortening of the absorption/scattering length proposed, further 919
strengthened by Ben Tam’s ex-situ absorption measurements with scintillator 920
taken from the detector, as well as knowledge about a likely “cooking” of PPO 921
during the PPO-fill. 922

- Describe the provisional optics model decided on based on these measurements, which includes an additional non-re-emitting component of the scintillator. 923
 - As a further cross-check, SMELLIE should be sensitive to changes in the overall extinction length of the scintillator, especially for short extinction lengths relative to the size of the detector. 925
926
927
 - More straightforward in measuring extinction length compared to scattering length — no need to distinguish between scintillator re-emission and scattering. 928
929
 - Further uses: can be used to monitor the extinction length over time! 930
- [4 pages] 931

5.1.2 Analysis Approach

The 2-PMT Case

- Outline theoretical approach for how one could measure the extinction length of scintillator through a comparison of SMELLIE data between the scintillator and water phases, in the simplified 1 dimensional case with only 2 PMTs. 934
935
936

[3 pages]

937

Combining Results Between PMTs

- Not doing analysis with just 2 PMTs, of course! Can combine results from multiple PMTs within a beamspot: I explain how here. 939
940

[2 pages]

941

5.1 Extinction Length Analysis**59****Corrections Between the Water and Scintillator Phases**

942

- Note the complications that we have to deal with. Namely, the differing refractive indices of the media bending the beamspot differently in the phases, as well as the method used to estimate t_{emm} . 943
944
945
- Explain how we deal with these, the former through MC simulation. 946

[2 pages]

947

5.1.3 Validation of the Analysis in Simulation

948

- Show results of this approach being used to measure the extinction length in simulation. How well does it do? 949
950

[3 pages]

951

5.1.4 Results in Data

952

- Describe the data used in this analysis, both water and scintillator, which can be shown in a table. 953
954
- Show examples of analysis of data in action for 375 nm data: typical t_{res} distributions of backscattered and beamspot PMTs; calculation of that particular extinction length measurement, followed by the graph for extinction length in 375 nm over all fibres and time periods. 955
956
957
958
- Discuss what results can be seen in this plot: consistency between fibres, the expected change as a function of PPO concentration, and stability of the extinction length during the main 2.2 g/L scintillator phase. 959
960
961

- Compare results to those made by Ben ex-situ: are they in agreement? If not, what possible systematics could there be? The main one for my analysis is likely to be uncertainties in the simulated beam profile that leak through into the refractive index correction of the beamspot. For the ex-situ analysis, the value of the extinction length obtained is achieved through background subtraction at some long wavelength, and the particular choice of this wavelength can lead to systematic changes in the obtained extinction length. 962
963
964
965
966
967
968
- Look at results at longer wavelengths: can anything reasonably be said at these longer wavelengths? Why/why not? 969
970
- Finally: describe any conclusions that can be reached, in particular whether we can affirm the optics model we use in RAT. 971
972

[8 pages]

973

5.2 Scattering Analysis

974

5.2.1 Historical Approaches and the Problem of Systematics

- Comparison to MC is necessary in scattering analysis, compared to merely being needed as a correction factor. This is because of the angular dependence of scattering. As a result, we can be far more susceptible to systematics from poor modelling! 976
977
978
979
- As a warning, show how Krish's/Esther's approach to the SMELLIE scattering analysis suffers majorly from these systematic effects. Requires describing their analysis approach briefly, and then explaining how the systematics described in Section ?? lead to major problems with this approach. 980
981
982
983

5.2 Scattering Analysis**61**

- Motivates the need for either reduced systematics, or an alternative analysis approach that is more robust to them! 984
985

[2 pages]

986

5.2.2 New Methodology

987

Signal Region Selection

988

- Propose the new analysis approach: looking at light in the “bad light-path” PMT region. Define what this region is. 989
990
- Give qualitative argument for why we expect this region to be robust to the beam profile systematics: dominated by the scattered signal as no direct light can make it here, and changes to beam profile should get “smeared out” after scattering. 991
992
993
994
- Show how simulations indicate this should be a region with a very high purity of scattered light, and (assuming all else being equal) robust to beam profile uncertainties. 995
996
997
- Confirm robustness of selected PMT region to uncertainties in AV offset and fibre position. 998
999

[5 pages]

1000

Measuring the Emission Intensity

1001

- Remaining systematics is now in the calculation of an average absolute emission intensity. 1002
1003

62

Analysis of SMELLIE Data in the Scintillator Phase

- Show how various methods don't work particularly well: whole detector npe, ¹⁰⁰⁴ beamspot npe, backscattered light npe, "bad light-path" PMTs but at later times. ¹⁰⁰⁵ Explain why it goes wrong for each method. ¹⁰⁰⁶
- Look at "beamspot but excepting the central bit": if that works well, then we ¹⁰⁰⁷ can continue! ¹⁰⁰⁸
- Otherwise, we'll have to live with measuring relative scattering lengths instead ¹⁰⁰⁹ of absolute amounts, using the outer water back-scattering as a measure of the ¹⁰¹⁰ relative emission intensity. ¹⁰¹¹

[4 pages]

¹⁰¹²

5.2.3 Results

¹⁰¹³

- Actually do the proposed analysis on data, versus time and wavelength. Do the ¹⁰¹⁴ results seem consistent between fibres? Are they sensible values? ¹⁰¹⁵

[5 pages] [33 PAGES TOTAL]

¹⁰¹⁶

Chapter 6

1017

Solar Oscillation Analysis

1018

Driving out into the Sun

Let the ultraviolet cover me up

Looking for a Creation Myth

Ended up with a pair of black lips

1019

This is the End

PHOEBE BRIDGERS

Measuring the “solar” neutrino oscillation parameters Δm_{21}^2 and θ_{12} is one of the 1020 principal aims of the SNO+ detector during the scintillator-phase. There are, in 1021 fact, two complementary methods of measuring these parameters: the oscillations of 1022 anti-neutrinos from terrestrial nuclear reactors, and the oscillations of neutrinos from 1023 the Sun. 1024

This chapter focuses on the latter approach, using ${}^8\text{B}$ neutrinos coming from the 1025 Sun to measure the solar oscillation parameters. An initial background-free study was 1026 performed by Javi Caravaca [?], which demonstrated that it was indeed possible 1027 to make such a measurement in the detector. The work in this chapter builds on 1028 substantially from that analysis. This chapter also draws on the associated reactor 1029

anti-neutrino analysis built by Iwan Morton-Blake [?], and more broadly from the ¹⁰³⁰ general techniques used in the $0\nu\beta\beta$ analysis of Tereza Kroupova [?] and Jack ¹⁰³¹ Dunger [?]. ¹⁰³²

This chapter begins by explaining how it is possible to measure the solar oscillation ¹⁰³³ parameters via ^8B events. Then, the framework used to perform the analysis is then ¹⁰³⁴ explained: that of a *Bayesian Analysis using Markov Chain Monte Carlo techniques*. ¹⁰³⁵ After the method has been described, the dataset upon which the analysis is performed ¹⁰³⁶ is then introduced. The results and associated validation are then given. Given these ¹⁰³⁷ results, a projection is then made for the expected sensitivity to θ_{12} as a function of ¹⁰³⁸ livetime. ¹⁰³⁹

6.1 Analysis Methodology

1040

6.1.1 Observational Principle

1041

How can we measure neutrino oscillation parameters via solar neutrinos in the SNO+ ¹⁰⁴² detector? As discussed in Chapter ??, it is possible to detect all flavours of neutrino ¹⁰⁴³ through elastic scattering with electrons in the detector. If this interaction was purely ¹⁰⁴⁴ neutral-current, then there would be no way of telling the flavour-state of an interacting ¹⁰⁴⁵ neutrino. However, electron neutrinos are able to interact through an additional ¹⁰⁴⁶ charged-current mode. This modifies the cross-section for electron neutrinos, and ¹⁰⁴⁷ means that as the survival probability for electron neutrinos generated from the Sun, ¹⁰⁴⁸ P_{ee} , is modified, the interaction probability of neutrinos with the detector will also. ¹⁰⁴⁹

Of course, we do not directly measure neutrino energies in the detector — only ¹⁰⁵⁰ the associated scattered electron. If there were no correlation between the observed ¹⁰⁵¹ electron energy and its associated neutrino, then the only effect of neutrino oscillations ¹⁰⁵² would be to change the overall observed rate of events due to this process. There ¹⁰⁵³

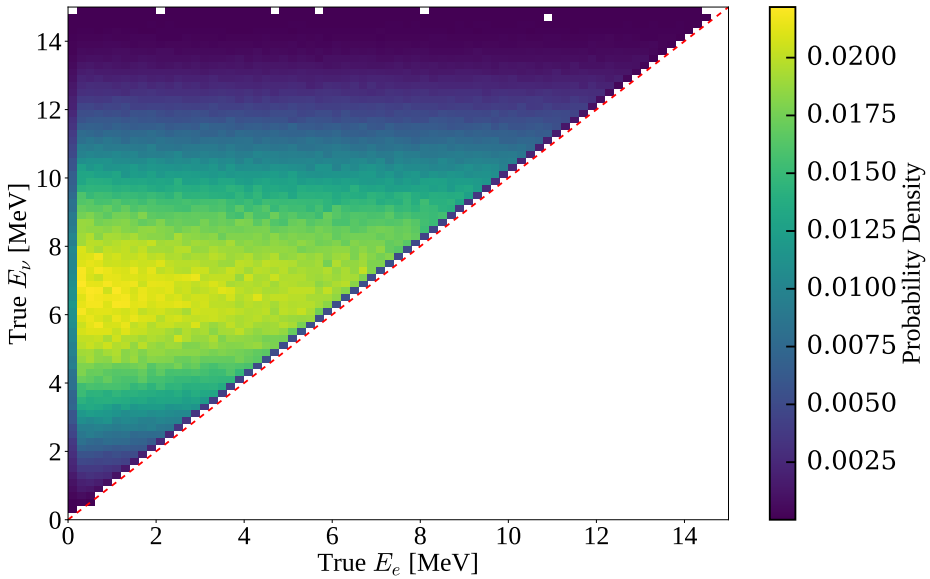


Fig. 6.1: 2D probability distribution comparing the true neutrino energy from a ${}^8\text{B}$ ν_e to the true energy of the scattered electron. Also shown in red is the line $E_\nu = E_e$.

would be no change in the shape of the event's energy spectrum, even though neutrino oscillations are a function of neutrino energy. Fortunately, there is some dependence of the neutrino's energy, E_ν on that of the scattered electron, E_e . This dependence can be seen in Fig. ?? for ${}^8\text{B}$ electron neutrinos interacting in SNO+. As can be seen, the dependence is weak, and comes mostly from basic energy conservation: If one observes a 10 MeV electron event in the detector, it can't reasonably have come from a 5 MeV neutrino.

In Fig. ?? we can see the impact each physical process has on the energy spectrum that we eventually observe. We start with a broad energy distribution of ${}^8\text{B}$ electron neutrinos generated in the Sun. These neutrinos then oscillate their flavour state as they propagate to the detector, in an energy-dependent manner. When a (tiny) fraction of these neutrinos interact with the electrons in our detector, there is both an energy- and flavour-dependence on the cross-section. The scattered electrons gain a kinetic energy with some mild dependence on the inciting neutrino's energy, which is then measured by the detector to within some energy resolution.

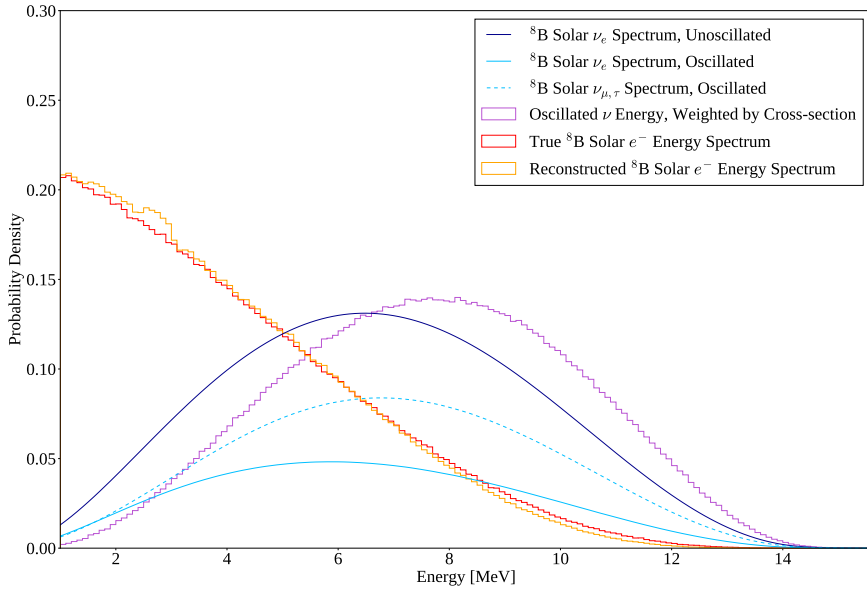


Fig. 6.2: The evolution of energy distributions related to ${}^8\text{B}$ solar neutrino detection. The unoscillated neutrino spectrum is taken from [?]; neutrino oscillations assume oscillation parameters from the current global fit results [?] and ν_e survival probabilities calculated via the method described in Section ???. The latter three distributions were obtained from MC production as described in Section ???, with the cross-section formula coming from [?].

Fig. 6.3

Let us now consider the dependence of P_{ee} on the individual neutrino oscillation parameters. Recall from Eq. ?? that, after considering matter-induced oscillations due to neutrinos passing through the Sun and possibly the Earth, $P_{ee} = {}^{1069}$ $P_{ee}(\tan 2\theta_{12}^M, \sin \theta_{13}^M, \Delta m_{21,M}^2) = P_{ee}(\theta_{12}, \theta_{13}, \Delta m_{12}^2, \Delta m_{13}^2)$. Fig. ?? shows the dependence of each of these four oscillation parameters on $P_{ee}(E)$. We can see that in reality 1070 only the two parameters Δm_{21}^2 and θ_{12} have a substantial impact on $P_{ee}(E)$ and hence 1071 the observed electron energy spectrum. Because of this, for this analysis we will only 1072 ever vary these two oscillation parameters, and keep θ_{13} and Δm_{13}^2 at their current 1073 global fit values¹ of $\sin^2 \theta_{13} = 0.0222$ and $\Delta m_{13}^2 = +2.515 \times 10^{-3} \text{ eV}^2$ [?]. 1074 1075 1076 1077

¹We use the global fit results excluding Super-Kamiokande's atmospheric data, and assuming normal ordering of the neutrino mass hierarchy. This choice has a tiny impact on the magnitudes of these two fixed parameters, the main impact being the sign of Δm_{13}^2 .

6.1.2 Background Processes

1078

Sadly, elastically-scattered electrons from ^8B neutrinos are not the only events we 1079 see in the SNO+ detector during the scintillator phase. There are a number of 1080 background processes that our signal must compete against. Below a reconstructed 1081 energy of $\sim 2.5 \text{ MeV}$, it is known that various backgrounds completely swamp any 1082 possible ^8B signal, and so for this analysis we only consider processes that can generate 1083 reconstructed energies of at least $E_{\min} = 2.5 \text{ MeV}$. The following subsections explain 1084 each of these backgrounds, as well as methods that have been used to mitigate them 1085 as much as possible. 1086

Internal Uranium- and Thorium-Chain Backgrounds

1087

Although every effort has been made to make the scintillator cocktail that fills SNO+ 1088 to be as radio-pure as possible, there inevitably remain trace amounts of the radioactive 1089 isotopes that derive from the decay chains of the ^{238}U and ^{232}Th isotopes. Fig. ?? 1090 shows these two decay chains. Fortunately, only a fraction of the radioactive isotopes 1091 in these chains actually are capable of generating events in the detector with energies 1092 above E_{\min} : these have been highlighted in Fig. ?? in gold. 1093

Of particular note are the decays of ^{212}Bi and ^{214}Bi . Both are capable of either α - or 1094 β -decays to Tl or Po isotopes, respectively. For the former, it is the subsequent β -decay 1095 of the Tl that can have a reconstructed energy above E_{\min} . For the latter, the Bi 1096 decay is the part of the pair of decays that can lie above E_{\min} . Although the α -decays 1097 here certainly have Q-values well above 2.5 MeV, the liquid scintillator quenches the 1098 observed energy well below E_{\min} . The so-called “Bi–Po” decays are particularly special 1099 because the lifetimes of ^{212}Po and ^{214}Po are 300 ns and 164 μs , respectively, which are 1100 short enough to allow for highly-effective coincidence tagging. 1101

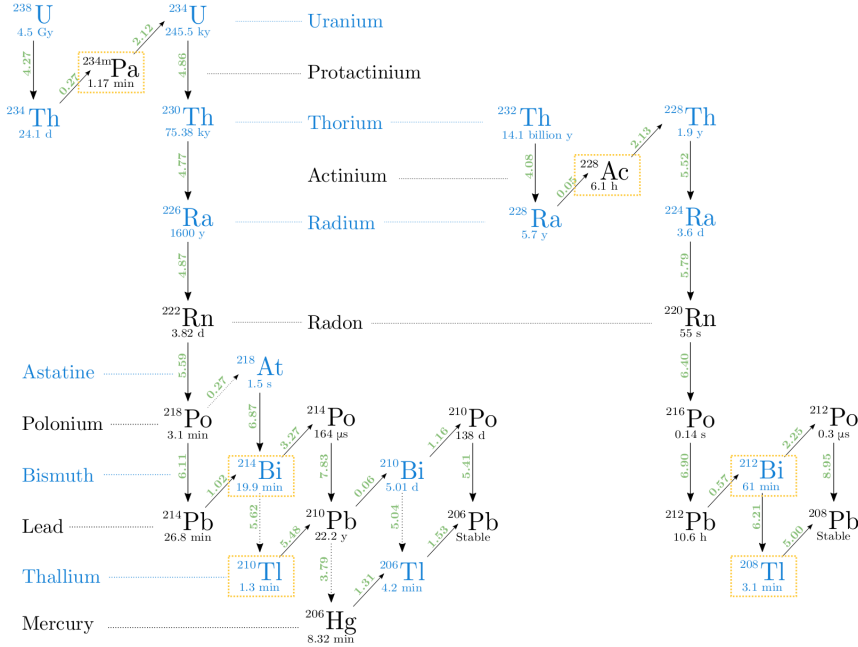


Fig. 6.4: The ^{238}U and ^{232}Th decay chains, taken from [?]. Isotopic half-lives are given below their symbol; the Q-values for each decay, in MeV, is given in green. Downward arrows indicate an α -decay; diagonal arrows indicate β -decay. Isotopes highlighted in gold are potential backgrounds for this solar analysis.

There are two classes of Bi–Po event in the detector: “out-of-window” events 1102 for which the Bi and Po occur in separate event windows, and “in-window” events 1103 whereby the Bi and Po occur within the same event window. These lead to two distinct 1104 strategies for tagging these kinds of events. For out-of-window Bi–Pos, we look for 1105 a delayed coincidence of two events. Using the tagging algorithm suggested in [] as 1106 a starting point, the chosen procedure was as follows. There must be two events 1107 that trigger the detector within $4\ \mu\text{s}$ of one another, and both have a valid `scintFit` 1108 position reconstruction within 2 m of one another. The delayed candidate event must 1109 also have at least 100 cleaned PMT hits. This very broad coincidence tagging procedure 1110 was designed to ensure that the cut was as *efficient* in tagging (and hence, rejecting) 1111 Bi–Pos as possible, whilst negligibly impacting the solar signal. This is in contrast to 1112 the cuts chosen by Rafael Hunt-Stokes in [], which try and obtain a highly *pure* sample 1113 of Bi–Po tags. 1114

Fig. 6.5

Of course, the above delayed coincidence procedure cannot catch any of the in-¹¹¹⁵ window Bi–Po events. For these, we use a different approach. Because two decays¹¹¹⁶ happened in the same event window, we expect to see two distinct peaks in the event’s¹¹¹⁷ time residual spectrum. In order to look for this event topology, a likelihood-ratio¹¹¹⁸ classifier was run over events, first developed by Eric Marzec [] and re-coordinated for¹¹¹⁹ the 2.2 g l⁻¹ LABPPO scintillator optics by Ziping Ye []. This classifier calculates the¹¹²⁰ likelihood ratio between the null hypothesis of a $0\nu\beta\beta$ event (a proxy in this analysis for¹¹²¹ single-site events such as our ^8B signal) and the alternative hypothesis of an in-window¹¹²² Bi–Po event. The more negative the value of the result, **alphabeta212**, the greater¹¹²³ the evidence there is for rejecting the null hypothesis of a single-site event. Events¹¹²⁴ with $\text{alphabeta212} < 0$ were then rejected.¹¹²⁵

Combining both out-of-window and in-window Bi–Po tagging, the impact on¹¹²⁶ ^{212}Bi –Po,²¹⁴Bi–Po, and ^8B ν_e events can be seen in Fig. ???. We consider here only¹¹²⁷ events that pass all other cuts used in this analysis: see Section ?? for the specifics¹¹²⁸ of the cuts used. Because of the different lifetimes of the decays,²¹⁴Bi–Po decays¹¹²⁹ predominantly fall out-of-window whilst²¹²Bi–Po events are typically in-window. This¹¹³⁰ explains why the out-of-window tagging is substantially better at cutting²¹⁴Bi–Po¹¹³¹ decays, whereas the in-window tagging far better tags²¹²Bi–Po decays. Overall, within¹¹³² the analysis region of interest (ROI), the two combined cuts are able to tag TODO%¹¹³³ of²¹⁴Bi–Po triggered events, TODO% of²¹²Bi–Po triggered events, whilst retaining¹¹³⁴ TODO% of ^8B ν_e signal events.¹¹³⁵

(α, n) Reactions

¹¹³⁶

The impact of ^{238}U - and ^{232}Th -chain isotopes does not simply end at their direct decays.¹¹³⁷ It is possible for the α s generated during these decays to undergo their own interactions¹¹³⁸

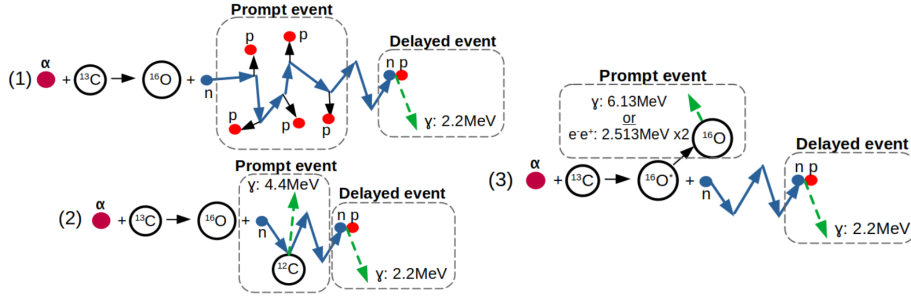


Fig. 6.6: Schematic of the three dominant modes of (α, n) interaction, taken from [?].

Fig. 6.7

with nuclei in the detector. Within the organic scintillator of SNO+, the dominant ¹¹³⁹ interaction of this type is when an α collides with a ${}^{13}\text{C}$ nucleus, emitting a neutron: ¹¹⁴⁰
 $\alpha + {}^{13}\text{C} \longrightarrow {}^{16}\text{O} + n$. This is known as an (α, n) reaction. ¹¹⁴¹

The topology of this reaction in the detector is a delayed coincidence, as shown ¹¹⁴² in Fig. ???. For the prompt signal, there is the light emitted from the α just before, ¹¹⁴³ and the n just after the (α, n) . The neutron then thermalises and gets captured by ¹¹⁴⁴ another nucleus — usually hydrogen in SNO+ — which creates an excited state that ¹¹⁴⁵ then eventually decays, creating a γ that creates the delayed signal in the detector ¹¹⁴⁶ [].

As can be seen in Fig. ???, (α, n) interactions can lead to events reconstructed ¹¹⁴⁷ at a wide variety of energies, which could be an issue for this analysis. However, ¹¹⁴⁸ because they are delayed coincidence events with a typical decay time of ~ 100 ns, ¹¹⁴⁹ the aforementioned out-of-window Bi–Po tagging algorithm also efficiently tags (α, n) ¹¹⁵⁰ events. Looking again at Fig. ??, simply by using the out-of-window Bi–Po tagger ¹¹⁵¹ without any further modifications TODO% of events in the ROI are cut. ¹¹⁵²

External Backgrounds

¹¹⁵³

All materials within the SNO+ detector are radioactive, not just the liquid scintillator ¹¹⁵⁴ cocktail. This includes the acrylic, ropes, external water, and PMTs. These components ¹¹⁵⁵

Fig. 6.8

have had their radiopurity “assayed” (that is, measured) throughout the detector’s lifetime, often back to the construction of the original SNO detector itself. The materials other than the liquid scintillator are known to have far higher background levels, especially in the important ^{238}U - and ^{232}Th -chain backgrounds [?]. To distinguish between the inherent backgrounds within the scintillator, and the backgrounds from materials at larger radii, we use the terminology “internal” and “external”, respectively.

Although there are numerous external backgrounds, with a suitably accurate and precise position reconstruction algorithm they can be suitably handled. The simplest approach is with a so-called “fiducial volume” (FV) cut: just throw out all events that reconstruct beyond some radius. The only external background events that will reach within the FV are those that have reconstructed very poorly, or have some long-distance radiation that manages to deposit radiation close to the centre of the AV. Because α and β radiation can only travel short distances through the detector, it is only γ radiation that can realistically travel far enough into the detector to be able to reconstruct anywhere near the centre. Moreover, the intensity of this γ radiation attenuates exponentially towards the centre of the detector, meaning only a tiny fraction of the total number of external events reconstruct within a 3.5 m FV, say. This strong radial-dependence can be seen in Fig. ??.

What this figure also demonstrates is that our solar signal has a completely different radial dependence to these backgrounds. As a result, if one considers not just the energy of events but also their reconstructed radius, then it is possible to get an additional handle on the external backgrounds. The FV cut can then be pushed further out to larger radii, allowing one to gain more signal statistics.

Work by Tereza Kroupova [?] allows for additional means of distinguishing external backgrounds from the solar signal. The underlying assumption in the reconstruction of

Fig. 6.9

SNO+ events is that there was an electron at a single point, which is entirely valid for ¹¹⁸¹
⁸B elastic scattering events. However, external backgrounds can fail this assumption in ¹¹⁸²
two ways. Firstly, these radioactive decays often generate γ radiation in addition to the ¹¹⁸³
main α/β particle, which creates a multi-site event. Because the `scintFit` position ¹¹⁸⁴
reconstruction algorithm is not prepared for a distribution of energy depositions in the ¹¹⁸⁵
scintillator, the t_{res} distribution will broaden. This allows an event classifier to be built ¹¹⁸⁶
that distinguishes between the t_{res} distributions of single-site events and externals, ¹¹⁸⁷
known as the “external background timing classifier”. Secondly, because external ¹¹⁸⁸
backgrounds that do reconstruct close to the centre of the detector typically have a γ ¹¹⁸⁹
that travelled a long distance towards the centre of the detector, we expect the earliest ¹¹⁹⁰
light that hits the PMTs to arrive most often along the direction of the reconstructed ¹¹⁹¹
position vector. A distribution of PMT hits for a given event as a function of their ¹¹⁹²
angular distribution relative to the direction of position reconstruction can be built, ¹¹⁹³
and compared to the expected distributions for single-site and external background ¹¹⁹⁴
events. This is known as the “external background topological classifier”. Much like ¹¹⁹⁵
the classifier described in Section ??, the single-site events used for comparison were ¹¹⁹⁶
 $0\nu\beta\beta$ events, but these have a similar single-site structure to the solar signal of interest ¹¹⁹⁷
in this analysis. ¹¹⁹⁸

Fig. ?? shows the correlation between the two classifier results for both a typical ¹¹⁹⁹
external background, and ⁸B ν_e events. ¹²⁰⁰

Cosmogenic Isotopes

1201

The final source of background events are radioactive isotopes that form via collisions of ¹²⁰²
cosmic rays with atomic nuclei, known as cosmogenic isotopes. Most of these isotopes ¹²⁰³
are short-lived [], with lifetimes $\mathcal{O}(1\text{s})$. Fortunately, the depth of SNO+ means that ¹²⁰⁴

6.1 Analysis Methodology

73

our rate of cosmic ray muons interacting with the detector is only 3 an hour []. Because ₁₂₀₅ the rate is so low relative to other experiments, relatively straightforward approaches ₁₂₀₆ to tagging and removing cosmic ray muons and their cosmogenic followers can be ₁₂₀₇ utilised without substantial loss of livetime. Events are tagged as a cosmic ray muon if ₁₂₀₈ they create a sufficient number of hits in the outward-looking PMTs above background ₁₂₀₉ levels, as well as many hits within the detector itself. The details of this tagging ₁₂₁₀ for the scintillator-fill were put in place by Lorna Nolan [], modifying the existing ₁₂₁₁ algorithms used in the water-phase [] and in SNO []. After a tagged cosmic muon ₁₂₁₂ event, all events for the next 20 s are then vetoed as a means of rejecting followers. ₁₂₁₃ This simple cut is enough to remove the vast majority of expected cosmogenic events ₁₂₁₄ in the scintillator-phase. The expected impact on loss of livetime, and hence quantity ₁₂₁₅ of signal events, is 3 lots of 20 s vetoes an hour, that is to say $1/60^{\text{th}}$ of the signal is ₁₂₁₆ lost via this cut. ₁₂₁₇

There is one cosmogenic isotope with a long-enough half-life that even the 20 s ₁₂₁₈ muon follower veto is not sufficient to remove all events. This is ^{11}C , which β^+ -decays ₁₂₁₉ to stable ^{11}B with a half-life of 20.4 min. The maximum possible energy deposited in ₁₂₂₀ this decay is 1.982 MeV [], just below E_{\min} , so only a small fraction of ^{11}C events end ₁₂₂₁ up in the ROI: the ones with very high energies that get their energy reconstruction ₁₂₂₂ falsely-inflated by some amount. As a result, this background is expected to be very ₁₂₂₃ much sub-dominant to all other backgrounds in this analysis. Because this background ₁₂₂₄ is important to consider for some other analyses, a triple-coincidence tagging algorithm ₁₂₂₅ is being built by Katharine Dixon [], but not used for this analysis currently. ₁₂₂₆

6.1.3 The Log-likelihood Test Statistic

₁₂₂₇

At the highest level, this analysis involves taking the data observed in the scintillator-fill ₁₂₂₈ after applying a certain set of cuts, along with simulated PDFs for all processes believed ₁₂₂₉

to build up the observed data with those same cuts applied, and then attempting to fit the combined energy and radial distributions of the MC to that of the data. Given a set of PDFs, to try and match the distribution of observables in data we can modify a number of parameters. These consist of the normalisations of each PDF (i.e. the total number of events observed due to that process), and any systematic parameters that could modify the shapes of these distributions. For this analysis, the neutrino oscillation parameters act as *de facto* systematic parameters, as they modify the shape of the ${}^8\text{B}$ PDFs. Of course, unlike usual systematics the oscillation parameters are what we are actively trying to measure, instead of being a nuisance.

In order to perform a fit to data in this way, we must first answer a set of questions:

1. Which signal and background processes must we consider?
2. In addition to their normalisations, are there any further parameters necessary to specify the distributions of the PDFs for each of the processes? Systematics and oscillation parameters are good examples.
3. What is our test statistic?
4. What algorithm do we use to try and find the best-fit result?
5. How do we measure uncertainties on these best-fit values for each parameter?

In section ??, question ?? was answered for this analysis. We now give the answer to question ??; all other questions on this list will be answered shortly.

The test statistic used for this analysis is the *binned extended log-likelihood*. Once the data and MC PDFs have been binned in both the observables of interest, it is assumed that the expected number of events in a given bin j is governed by a Poisson distribution:

$$P_j(n_j|\lambda_j) = \frac{\lambda_j^{n_j} e^{-\lambda_j}}{n_j!}, \quad (6.1)$$

6.1 Analysis Methodology

where $P_j(n_j|\lambda_j)$ is the probability of observing n_j events in bin j , given an expectation ₁₂₅₄ of λ_j events in total from signal and background processes in that bin. This λ_j can be ₁₂₅₅ decomposed into each of the expected rates for each process, i : ₁₂₅₆

$$\lambda_j = \sum_{i=1}^{N_{\text{PDFs}}} \mathcal{N}_i P_{ij}(\boldsymbol{\theta}), \quad (6.2) \quad 1257$$

where N_{PDF} is the number of PDFs being considered in the analysis, \mathcal{N}_i is the nor- ₁₂₅₈ malisation parameter of the i^{th} PDF, and $P_{ij}(\boldsymbol{\theta})$ is the probability of observing an ₁₂₅₉ event of process type j in bin i , assuming a set of non-normalisation parameters $\boldsymbol{\theta}$. By ₁₂₆₀ combining the probabilities of all the bins together, the total probability for a given ₁₂₆₁ set of processes assuming these parameters to give rise to the data seen is: ₁₂₆₂

$$P(\mathbf{n}|\mathcal{N}, \boldsymbol{\theta}) = L(\mathcal{N}, \boldsymbol{\theta}|\mathbf{n}) = \prod_{j=1}^{N_{\text{bins}}} \frac{\left[\sum_{i=1}^{N_{\text{PDFs}}} \mathcal{N}_i P_{ij}(\boldsymbol{\theta}) \right]^{n_j} e^{-\sum_{i=1}^{N_{\text{PDFs}}} \mathcal{N}_i P_{ij}(\boldsymbol{\theta})}}{n_j!}, \quad (6.3) \quad 1263 \\ 1264$$

where N_{bins} is the total number of bins being considered in the analysis. This probability ₁₂₆₅ can be re-framed as the likelihood of the vectors of parameters \mathcal{N} and $\boldsymbol{\theta}$ given ₁₂₆₆ the vector of number of events in each bin, \mathbf{n} : $L(\mathcal{N}, \boldsymbol{\theta}|\mathbf{n})$. It is rare to see the ₁₂₆₇ likelihood as-is, instead, for computational purposes the log-likelihood is used instead, ₁₂₆₈ $\mathcal{L}(\mathcal{N}, \boldsymbol{\theta}|\mathbf{n}) := \ln L(\mathcal{N}, \boldsymbol{\theta}|\mathbf{n})$. We can then get to the formula actually used for this ₁₂₆₉ analysis: ₁₂₇₀

$$\mathcal{L}(\mathcal{N}, \boldsymbol{\theta}|\mathbf{n}) = - \sum_{i=1}^{N_{\text{PDFs}}} \mathcal{N}_i + \sum_{j=1}^{N_{\text{bins}}} n_j \ln \left(\sum_{i=1}^{N_{\text{PDFs}}} \mathcal{N}_i P_{ij}(\boldsymbol{\theta}) \right). \quad (6.4) \quad 1271 \\ 1272$$

6.1.4 The Bayesian Statistical Approach

There are two main schools of statistical inference, “Frequentist” and “Bayesian”. In ₁₂₇₄ the former, probabilities describe the fraction of times a situation can be found within ₁₂₇₅ the whole ensemble of possible worlds. For the latter, we care not about an ensemble ₁₂₇₆

of worlds but instead our degree of belief in this current one. We update our beliefs as ¹²⁷⁷
we acquire knowledge of the world through Bayes' Theorem: ¹²⁷⁸

$$P(\boldsymbol{\mu}|\mathbf{x}) = \frac{\mathcal{L}(\boldsymbol{\mu}|\mathbf{x}) P(\boldsymbol{\mu})}{P(\mathbf{x})}. \quad (6.5) \quad ^{1279}$$

Here, $\boldsymbol{\mu}$ is the set of parameters that model our system, $P(\boldsymbol{\mu})$ is our *prior* (pre-existing) ¹²⁸⁰
distribution for those model parameters, and \mathbf{x} is the data taken in our experiment. The ¹²⁸¹
updated, *posterior* distribution $P(\boldsymbol{\mu}|\mathbf{x})$ is then the prior multiplied by the likelihood ¹²⁸²
of parameters $\boldsymbol{\mu}$ given observations \mathbf{x} , $L(\boldsymbol{\mu}|\mathbf{x})$, and divided by the total probability ¹²⁸³
 $P(\mathbf{x})$ of observing \mathbf{x} under any circumstance. ¹²⁸⁴

Both approaches to statistics are widely-used in statistical analysis, in both particle ¹²⁸⁵
physics and beyond. The Bayesian approach was used for this analysis, as it was ¹²⁸⁶
believed that this helps keep transparent what assumptions are being made in the ¹²⁸⁷
analysis. ¹²⁸⁸

Now, if one is able to determine the overall posterior distribution, then it is possible ¹²⁸⁹
to derive best-fit values with uncertainties for all parameters in the fit. This is done by ¹²⁹⁰
“marginalising” the posterior distribution, i.e. integrating over all parameters other ¹²⁹¹
than the one of interest. A sensible best-fit value is then the modal marginalised ¹²⁹²
posterior density, the highest value in the marginalised distribution. The uncertainty ¹²⁹³
on this value is derived from the spread of the marginalised posterior, by the calculation ¹²⁹⁴
of the 1σ Credible Interval (CI): this is the set of values for a given parameter which ¹²⁹⁵
has a total posterior probability of 68.3%, and contain the best-fit value. There are in ¹²⁹⁶
fact an infinite number of CIs that satisfy this property; for this analysis, the values ¹²⁹⁷
are chosen in decreasing order of marginalised posterior probability density. ¹²⁹⁸

6.1.5 Markov Chain Monte Carlo

1299

Of course, all of this assumes that one can accurately determine the posterior density 1300 distribution. Whilst the likelihood and prior distribution are straightforward enough 1301 to calculate, often-times $P(\mathbf{x})$ (which acts as a normalisation) is very challenging 1302 to determine. This is because calculating this normalisation involves integrating the 1303 likelihood over all the parameter space, and if there are a large number of parameters 1304 this can become enormously numerically complex. An alternative approach is needed! 1305

That alternative comes in the form of *Markov Chain Monte Carlo*, MCMC. A 1306 Markov Chain is any mathematical system for which the next state of the system is 1307 dependent only on its current state; the system is in some sense “memoryless”. For a 1308 large class of Markov Chains — those that are “ergodic” and “aperiodic” — one can 1309 prove that regardless of the initial position on the chain, the probability distribution 1310 converges to the same distribution []. MCMC uses such a Markov Chain which attempts 1311 to converge towards the posterior density distribution in particular. In MCMC, after 1312 choosing the initial position in the parameter space, successive states are chosen at 1313 random with a probability dependent only on the properties of the current position 1314 in parameter space and the proposed position. The convergence property of Markov 1315 Chains means that the set of steps made in the parameter space after some initial 1316 number of steps will have a distribution that converges to that of the posterior density 1317 distribution. 1318

There are a number of MCMC algorithms, and the particular one used in this 1319 analysis is that of the *Random-Walk Metropolis-Hastings Algorithm*. In this algorithm, 1320 after the initial position in the parameter space $\boldsymbol{\mu}$, a new step is proposed some distance 1321 from the current one, $\boldsymbol{\mu}'$. This step is chosen at random from a multivariate Gaussian 1322 distribution centred on the current position, with widths in each dimension of the 1323 parameter space chosen beforehand as constants for tuning the MCMC process. This 1324

choosing of a new proposed step at random is what gives the algorithm its Monte Carlo ¹³²⁵ and Random Walk titles. Once a new step is proposed, it is accepted as the new step ¹³²⁶ with a probability $S(\boldsymbol{\mu}'|\boldsymbol{\mu})$ according to the condition of *detailed balance*: ¹³²⁷

$$\begin{aligned} S(\boldsymbol{\mu}'|\boldsymbol{\mu}) &= \min\left(1, \frac{P(\boldsymbol{\mu}'|\mathbf{x})}{P(\boldsymbol{\mu}|\mathbf{x})} \frac{R(\boldsymbol{\mu}|\boldsymbol{\mu}')}{R(\boldsymbol{\mu}'|\boldsymbol{\mu})}\right) = \min\left(1, \frac{L(\boldsymbol{\mu}'|\mathbf{x}) P(\boldsymbol{\mu}')}{L(\boldsymbol{\mu}|\mathbf{x}) P(\boldsymbol{\mu})} \frac{R(\boldsymbol{\mu}|\boldsymbol{\mu}')}{R(\boldsymbol{\mu}'|\boldsymbol{\mu})}\right) \\ &= \min\left(1, \frac{R(\boldsymbol{\mu}|\boldsymbol{\mu}')}{R(\boldsymbol{\mu}'|\boldsymbol{\mu})} \exp\left[\mathcal{L}(\boldsymbol{\mu}'|\mathbf{x}) - \mathcal{L}(\boldsymbol{\mu}|\mathbf{x}) + \ln \frac{P(\boldsymbol{\mu}')}{P(\boldsymbol{\mu})}\right]\right). \end{aligned} \quad (6.6) \quad \begin{matrix} 1328 \\ 1329 \\ 1330 \end{matrix}$$

$R(\boldsymbol{\mu}'|\boldsymbol{\mu})$ is the probability density that position $\boldsymbol{\mu}'$ is proposed as a step from position $\boldsymbol{\mu}$, ¹³³¹ and vice versa for $R(\boldsymbol{\mu}|\boldsymbol{\mu}')$. In most cases, because of the use of the same multivariate ¹³³² Gaussian in choosing proposals, $\frac{R(\boldsymbol{\mu}|\boldsymbol{\mu}')}{R(\boldsymbol{\mu}'|\boldsymbol{\mu})} = 1$ simply. This component only becomes ¹³³³ important at the edges of the parameter space, preventing the sampling probability ¹³³⁴ being incorrectly impacted if a proposed step goes outside the allowed parameter space. ¹³³⁵

It is the detailed balance condition that ensures convergence of the MCMC algorithm ¹³³⁶ to specifically the posterior density distribution. Crucially, because it is only dependent ¹³³⁷ on the ratio of posterior densities, the hard-to-calculate normalisation $P(\mathbf{x})$ in both ¹³³⁸ posterior density terms cancels out, meaning one only needs to calculate the likelihood ¹³³⁹ and priors for each step, as well as $\frac{R(\boldsymbol{\mu}|\boldsymbol{\mu}')}{R(\boldsymbol{\mu}'|\boldsymbol{\mu})}$. ¹³⁴⁰

The specific implementation of MCMC used for this analysis is that of `OXO`, a ¹³⁴¹ C++ analysis framework first developed by Jack Dunger [?]. `OXO` is able to run ¹³⁴² the Metropolis-Hastings algorithm on multidimensional binned data, using the log- ¹³⁴³ likelihood defined in ???. This framework also allows one to include systematic parameters ¹³⁴⁴ that can float within the fit, and define non-uniform priors for normalisations and ¹³⁴⁵ systematics that have constraints: the details of this will be discussed shortly. ¹³⁴⁶

6.1.6 Choosing Priors

1347

For this analysis, the suggestions made by Biller & Oser in [?] about choosing prior distributions are followed: for parameters that do not have some pre-existing constraint, a flat prior is used. A nice consequence of this choice is that $\ln \frac{P(\mu')}{P(\mu)} = 0$, so the actual value of the prior for these variables never needs to be calculated when running the MCMC algorithm. For the bulk of this analysis, uniform priors are assumed on the neutrino oscillation parameters Δm_{21}^2 and θ_{12} , as the magnitudes of these parameters are now well-established.

1354

For parameters with existing asymmetric constraints $\beta_{-\sigma_-}^{+\sigma_+}$, this analysis uses an asymmetric Gaussian prior, equivalent to the logarithm of the prior being an asymmetric quadratic:

1357

$$\ln P(\mu) = \mathcal{A} - \begin{cases} \frac{(\mu-\beta)^2}{2\sigma_+^2} & \text{if } \mu \geq \beta, \\ \frac{(\mu-\beta)^2}{2\sigma_-^2} & \text{if } \mu < \beta. \end{cases} \quad (6.7) \quad 1358$$

Here, \mathcal{A} is the logarithm of the prior's normalisation constant, and cancels out in the detailed balance condition. For parameters with symmetric constraints, $\sigma_+ = \sigma_-$, then $\ln P(\mu)$ reduces to a quadratic with maximum at $\mu = \beta$.

1361

6.1.7 Including Systematics in the Fit

1362

One important implementation detail is how systematics are applied within the MCMC fitting process. Once systematics are added to the fit, at every step the binned PDFs for all the processes considered in the fit must get modified appropriately, which can become extremely computationally-intensive if not approached carefully. The strategy used in the `OXO` framework starts by thinking of the contents of a binned PDF as a vector of bin probabilities, $\mathbf{p} = (p_1, p_2, \dots, p_{N_{\text{bins}}})^T$. Then, we can think of a systematic acting on the PDF as a linear transformation, and hence a matrix S acting

1369

Fig. 6.10

on this vector: $\mathbf{p}' = S\mathbf{p}$. We only need to calculate this matrix once for a given set ₁₃₇₀ of systematic parameter values, and can then use the same matrix on all the PDFs ₁₃₇₁ in the fit. Furthermore, when multiple systematics are applied, the matrix for each ₁₃₇₂ systematic can then be combined via matrix multiplication into one single “detector ₁₃₇₃ response” matrix. OXO uses the **Armadillo** [] linear algebra package for efficient matrix ₁₃₇₄ manipulation. ₁₃₇₅

There is a problem that can arise when considering the impact of systematics ₁₃₇₆ near the edge of the analysis ROI. Many systematics such as shifts, scalings, and ₁₃₇₇ convolutions use information about the contents of nearby bins to determine the ₁₃₇₈ contents of a particular bin. However, for bins near the edge some of that information ₁₃₇₉ does not exist — it has been lost to the cuts that define the ROI. This can lead to a bias ₁₃₈₀ in the generation of the modified PDFs, and therefore also the posterior distribution. ₁₃₈₁

As an example, consider the impact of an energy scale systematic on the energy ₁₃₈₂ distribution of ^{234m}Pa events in the detector, shown in Fig. ???. Because the events ₁₃₈₃ seen for this process in the ROI are merely the high-energy tail, any systematic energy ₁₃₈₄ scaling $E'_{\text{reco}} := \beta E_{\text{reco}}$ should have a large impact on the number of events observed at ₁₃₈₅ the low end of the ROI. However, given that the information about data below E_{min} is ₁₃₈₆ lost to the ROI cuts, any energy scaling of $\beta > 1$ will not be applied correctly at all. ₁₃₈₇

The solution to this problem is defining a “buffer region” of bins on either side of ₁₃₈₈ the ROI, which allow for tracking of events in and out of the ROI due to systematics, ₁₃₈₉ but aren’t considered when calculating the likelihood. This is also shown in Fig. ???. ₁₃₉₀ After the scaling systematic is applied, although incorrect bin values are found in the ₁₃₉₁ buffer region, this is fine because we are no longer calculating the likelihood with those ₁₃₉₂ bins. Note that because of this modification, the normalisation parameters we put into ₁₃₉₃ the model no longer represent the expected number of events in the ROI. Instead, they ₁₃₉₄

represent the number of events expected in both the ROI and buffer region, before any 1395
systematics have been applied. 1396

6.1.8 Including Oscillations in the Fit

1397

Within the analysis MCMC code, the process of neutrino oscillations are thought of 1398
as a *de facto* systematic that acts only on the ${}^8\text{B}$ ν_e and ν_x signal spectra. Three 1399
parameters relevant to the signal are floated within the MCMC fit: Δm_{21}^2 , θ_{12} , and 1400
 Φ_{sB} , the unoscillated ${}^8\text{B}$ flux relative to the expected rate. For the two signal PDFs, a 1401
third “bookkeeping” dimension is added on top of reconstructed energy and radius: 1402
the true neutrino energy, E_ν . This is necessary for correctly applying oscillations, as 1403
the oscillation probability is a function of the neutrino’s energy, not the scattered 1404
electron’s. Before the fit, these 3D PDFs are given normalisations corresponding to 1405
the expectation of the number of events for each type, ν_e and ν_x , after cuts but before 1406
oscillations have been applied. Strictly speaking there should be zero ν_x events before 1407
neutrino oscillations: the pre-oscillation rate used here is the post-cut number of events 1408
expected if 100% of the neutrinos oscillated to the ν_x type. 1409

During the MCMC fit, for a given set of parameters $\boldsymbol{\theta} = (\Delta m_{21}^2, \theta_{12}, \Phi_{\text{sB}})$ the 1410
following is performed to oscillate the signal PDFs. Firstly, the normalisations are scaled 1411
by the factor Φ_{sB} . Then, for each E_ν bin the survival probability $P_{ee}(E_\nu, \Delta m_{21}^2, \theta_{12})$ is 1412
calculated. Each bin then has their probability scaled by either P_{ee} or $1 - P_{ee}$, for ν_e and 1413
 ν_x respectively. Of course, within the structure of the **OXO** framework these bin-by-bin 1414
scaling aren’t immediately applied, but instead a matrix describing the impact of 1415
oscillations on each of the PDFs is made. Because the oscillation transformation is 1416
purely a bin-by-bin scaling, the resulting matrices are diagonal, with diagonal elements 1417
 $\Phi_{\text{sB}} \cdot P_{ee}(E_\nu, \Delta m_{21}^2, \theta_{12})$ or $\Phi_{\text{sB}} \cdot (1 - P_{ee}(E_\nu, \Delta m_{21}^2, \theta_{12}))$ for ν_e and ν_x respectively. 1418
After the oscillation matrix along with all other systematic matrices are applied to the 1419

signal PDFs, the PDFs are then marginalised over the E_ν dimension so that the signal ¹⁴²⁰
PDFs match the dimensionality of all other processes. ¹⁴²¹

Calculations of the survival probability are handled with **PSelmaa**, an algorithm ¹⁴²²
written by Nuno Barros for the SNO 3-phase Analysis ¹⁴²³. This considers not only the
neutrino oscillations through the vacuum of space between the Sun and Earth, but also ¹⁴²⁴
the impact of matter effects in both the Sun and Earth. This can usually be a very ¹⁴²⁵
computationally-intensive process, but **PSelmaa** takes advantage of the assumption ¹⁴²⁶
that the solar oscillation parameters are in the so-called “Large Mixing Angle” regime, ¹⁴²⁷
making the calculation much faster. As seen in Section ??, previous solar oscillation ¹⁴²⁸
experiments demonstrate that this assumption is reasonable. For this analysis, the ¹⁴²⁹
standard MSW effect is assumed with neutrinos obeying the Normal Hierarchy, with ¹⁴³⁰
the Sun following the **B16_GS98** metallicity model ¹⁴³¹ and the **PREM** model being used ¹⁴³²
for the Earth ¹⁴³³.

One final thing **PSelmaa** needs to know to calculate survival probabilities is the ¹⁴³³
distribution of solar zenith angles during the data-taking. The solar zenith θ_z is the ¹⁴³⁴
angle between the two following vectors: one going from the centre of the Earth through ¹⁴³⁵
the centre of the SNO+ detector, and another starting from the detector’s centre and ¹⁴³⁶
pointing towards the Sun. As an example, if the Sun were ever to be directly overhead ¹⁴³⁷
the detector, both vectors would be along direction \hat{z} in detector coordinates, leading ¹⁴³⁸
to a solar zenith angle of $\theta_z = 0$. The position of the SNO+ detector on Earth, as ¹⁴³⁹
well as the times at which the detector was live, determine the solar zenith angle ¹⁴⁴⁰
distribution. If not accounted for, this can lead to a bias in the result of the analysis, ¹⁴⁴¹
as a preponderance of livetime taken at night (say) would lead to a larger fraction of ¹⁴⁴²
solar neutrinos having to pass through the bulk of the Earth to get to the detector, ¹⁴⁴³
and hence the impact of the MSW effect would be greater. ¹⁴⁴⁴

6.2 Analysis on Scintillator-Phase data

83

Even after using the Large Mixing Angle approximation, having to call `PSelmaa` 1445 numerous times for every step in the MCMC algorithm would lead to exorbitant run 1446 times for the fitting. Therefore, a further approximation is made. Before running the 1447 MCMC fit, `PSelmaa` is used to calculate P_{ee} over the necessary 3D space of parameters. 1448 To get a fine scan of this space, 101 E_ν values from 1 MeV to 20 MeV, 101 Δm_{21}^2 values 1449 from 3×10^{-6} eV² to 1×10^{-3} eV², and 151 values for θ_{12} from 5° to 65° were looked 1450 over. This 3D grid of $101 \cdot 101 \cdot 151$ P_{ee} values is then written to disk, and loaded 1451 into memory for use during the fit as a lookup table. At run-time, as the Metropolis- 1452 Hastings algorithm samples this 3D space the survival probability is estimated through 1453 a trilinear interpolation of the 3D grid loaded in: a version of linear interpolation for 1454 three dimensions []. 1455

[19 pages currently, without figures; probably +5 pages for figures.] 1456

6.2 Analysis on Scintillator-Phase data

1457

6.2.1 Dataset and Livetime

1458

- Description of dataset chosen for analysis: 2.2 g/L scintillator-phase data that 1459 satisfies the “gold” list of run selection requirements, between May and November 1460 2022. 1461
- Explain requirements for run being selected into the Gold list. 1462
- Note ‘raw’ livetime calculated for this dataset, and then calculate the impact 1463 that the muon and high-nhit vetos have on the livetime. 1464
- Note which RAT versions MC production is being used to compare to data. 1465

[2 pages]

1466

6.2.2 Event Selection

1467

- List final set of cuts chosen for analysis, along with any explanations for cuts that haven't already been motivated earlier (e.g. data cleaning). These are:
 - Event index cut (prevents MC events that don't trigger detector from being used) 1468
 - Data cleaning cuts 1469
 - High-nhit event timing veto cut 1470
 - Valid scintFit reconstruction 1471
 - Reconstructed energy $2 < E < 14$ 1472
 - Radial fiducial volume cut 1473
 - BiPo out-of-window tag 1474
 - BiPo in-window classifier cut 1475
 - Externals classifier cut 1476
 - “Cleanliness” cut 1477
 - Position FOM cut 1478
- Show impact of cuts on data and MC. Show tables (the full details maybe in an appendix) indicating this. 1479
- Describe the finalised choice of binning for PDFs and data. 1480

[4 pages]

1481

6.2.3 Expected Rates and Constraints

1482

- Show expected rates calculation for both signal and background. 1483

6.2 Analysis on Scintillator-Phase data

85

- Describe the constraints chosen to apply to the fit, and why they can be justified. 1488

These are:

1489

- B8 flux constraint 1490
- U-238 and Th-232 constraints from BiPo tagging 1491
- Alpha-n constraint from Po-210 tagging by Serena and Shengzhao 1492
- External constraints from Tony Zummico's water-phase externals analysis. 1493
- Describe the systematics to be added to the fit (just energy scale for now, maybe 1494
also energy smearing?). For other possible systematics, such as those in position, 1495
my aim is to explain why they are sub-dominant and so don't need to be added 1496
to the fit. Will cover more about impact of systematics in the next subsection. 1497

[4 pages]

1498

6.2.4 Results

1499

Fit Validation

1500

- Show plots of parameter values versus step, to demonstrate that the step sizes 1501
have been tuned sufficiently. 1502
- Show auto-correlation plots, to motivate a sensible “burn-in” size. 1503
- Posterior density plots for each nuisance parameter, to check that they all look 1504
sensible and have sufficient statistics. 1505
- Show plot of correlation coefficients between parameters, and note any strongly- 1506
correlated parameters. 1507

[6 pages]

1508

Oscillation Fit Results

1509

- Look at the data versus ‘best-fit’ MC plot in energy, radius, and both. (Recall 1510 that in MCMC, the ‘best-fit’ is not the point of parameter scape reached at the 1511 end, but the point of highest posterior density). Is there a good fit to data? Any 1512 clear disagreements? 1513
- Show 2D contour plot for oscillation parameter posterior density. Note salient 1514 features. Show 1D posterior densities for each oscillation parameter. Derive mea- 1515 surement result for θ_{12} , i.e. point of highest posterior density, with uncertainties 1516 given by the 1σ credible interval. 1517

[5 pages]

1518

Impact of Systematics

1519

- Show impact of modifying certain constraints on the final results of the measure- 1520 ment of θ_{12} . In particular: fiducial volume, ${}^8\text{B}$ flux constraint. 1521
- Discussion of systematics post-fit — Hopefully energy scaling parameter should 1522 be close to 1, given the Collaboration’s calibration of the optics (light yield in 1523 particular). Perform a scan over energy smearing, and check impact of possible 1524 radial scale systematic. 1525

[8 pages]

1526

6.3 Sensitivity Projections

1527

- Using the same production MC, generate PDFs with the expected normalisations 1528 for longer periods of livetime: 1, 3, and 5 years. This still assumes a scintillator-fill 1529

6.3 Sensitivity Projections

87

with identical detector conditions on average, so not considering the impact ₁₅₃₀
BisMSB loading at any point. ₁₅₃₁

- Describe any further constraints to be assumed on top of the existing analysis ₁₅₃₂
of data: expected improved constraints on various backgrounds, as well as a ₁₅₃₃
possible energy-scale calibration constraint from the AmBe source or an internally- ₁₅₃₄
deployed source, for example. ₁₅₃₅
- Run MCMC fits to these Asimov PDFs for each livetime scenario. Describe ₁₅₃₆
results in terms of the improvement to the sensitivity to θ_{12} as a function of ₁₅₃₇
livetime. ₁₅₃₈
- Also consider scenario of lower backgrounds! How does that impact the result? ₁₅₃₉
- Could consider scenario of BisMSB deployment, leading to substantially greater ₁₅₄₀
light yield and hence energy resolution. Given time it would take for Production ₁₅₄₁
MC to be generated for this scenario, I would likely have to come up with ₁₅₄₂
something clever and quick to actually do this. There quite possibly won't be ₁₅₄₃
enough time. ₁₅₄₄

[8 pages]

₁₅₄₅

[61 PAGES TOTAL]

₁₅₄₆

Chapter 7

1547

Conclusions and Suggestions for

1548

Future Work

1549

- Say what has been achieved in this thesis! In particular:
 - Substantial improvement to the SMELLIE generator in terms of speed and dynamic range 1550
 - A much stronger understanding of the discrepancies between data and MC in SMELLIE 1551
 - The creation of two analyses of SMELLIE data, designed explicitly around being robust to these systematics 1552
 - A measurement of the extinction length of scintillator *in-situ* with SMELLIE at 375 nm, monitored over time 1553
 - A first measurement of the scattering length of the scintillator *in-situ*, monitored over time 1554
 - The creation of an analysis of ${}^8\text{B}$ solar neutrinos in the scintillator phase to measure the solar neutrino oscillation parameters 1555

- The first measurement of θ_{12} using ^8B neutrinos in SNO+ 1563
- Projections of this solar analysis' precision at longer livetimes 1564
- Give suggestions for further work that could be done on both SMELLIE and the solar oscillation analysis: 1565
 - Inclusion of LABPPO's polarisability anisotropy in the detector's optical scattering simulation, and determination of its impact on both Physics and SMELLIE measurements 1566156715681569
 - Further investigation of SMELLIE's wavelength-dependence of the beam profiles, looking both at possible origins for the phenomenon and correcting for this in simulation 157015711572
 - Various computational improvements to allow for faster MCMC run-times, including the calculation of the systematic matrices, and possible use of GPUs to parallelise some parts of the computation. 157315741575
 - Inclusion of additional solar neutrino components at lower energy into the fit, e.g. Be7. Maybe the addition of lower energies also helps to naturally constrain backgrounds within the fit? 157615771578
 - Looking at the impact of various advanced background-rejection procedures, such as event directionality or topology. How much do they help with the sensitivity? 157915801581
 - Looking at the impact of splitting data into day and night parts, to try and provide further constraints on any matter effects. Not expected to be significant, so was ignored for this analysis so far. 158215831584
 - Performing a combined fit with the reactor anti-neutrino oscillation analysis, which allows for the handling of correlated uncertainties, such as detector response systematics. 158515861587

[3 PAGES TOTAL]

1588

References

1589

- [1] SNO+, V. Albanese *et al.*, The SNO+ experiment, Journal of Instrumentation **16**, P08059 (2021). 1590
1591
- [2] K. Majumdar, *On the Measurement of Optical Scattering and Studies of Background Rejection in the SNO+ Detector*, DPhil Thesis, University of Oxford, 2015. 1592
1593
1594
- [3] E. Turner, *A Measurement of Scattering Characteristics of the Detection Medium in the SNO+ Detector*, DPhil Thesis, University of Oxford, 2022. 1595
1596
- [4] SNO+, M. Anderson *et al.*, Optical calibration of the SNO+ detector in the water phase with deployed sources, Journal of Instrumentation **16**, P10021 (2021). 1597
1598
- [5] S. S. Wilks, The Large-Sample Distribution of the Likelihood Ratio for Testing Composite Hypotheses, The Annals of Mathematical Statistics **9**, 60 (1938). 1599
1600
- [6] J. Caravaca, SNO+ Sensitivity to Standard Solar Neutrino Oscillations, 2020. 1601
- [7] I. Morton-Blake, *First Measurement of Reactor Antineutrinos in Scintillator at SNO+ and Study of Alternative Designs for Large-Scale Liquid Scintillator Detectors*, DPhil Thesis, University of Oxford, 2021. 1602
1603
1604
- [8] T. Kroupová, *Improving the Sensitivity to Neutrinoless Double Beta Decay in SNO+*, DPhil Thesis, University of Oxford, 2020. 1605
1606
- [9] J. Dunger, *Topological and Time Based Event Classification for Neutrinoless Double Beta Decay in Liquid Scintillator*, DPhil Thesis, University of Oxford, 2018. 1607
1608
1609
- [10] W. T. Winter, S. J. Freedman, K. E. Rehm, and J. P. Schiffer, The B8 Neutrino Spectrum, Physical Review C **73**, 025503 (2006), arxiv:nucl-ex/0406019. 1610
1611
- [11] I. Esteban, M. Gonzalez-Garcia, M. Maltoni, T. Schwetz, and A. Zhou, The fate of hints: Updated global analysis of three-flavor neutrino oscillations, Journal of High Energy Physics **2020**, 178 (2020). 1612
1613
1614
- [12] J. N. Bahcall, M. Kamionkowski, and A. Sirlin, Solar neutrinos: Radiative corrections in neutrino-electron scattering experiments, Physical Review D **51**, 6146 (1995). 1615
1616
1617
- [13] SNO+, S. Andringa *et al.*, Current Status and Future Prospects of the SNO+ Experiment, Advances in High Energy Physics **2016**, 1 (2016). 1618
1619

- [14] S. D. Biller and S. M. Oser, Another look at confidence intervals: Proposal for a more relevant and transparent approach, Nuclear Instruments and Methods in Physics Research Section A: Accelerators, Spectrometers, Detectors and Associated Equipment **774**, 103 (2015). 1620
1621
1622
1623